ISSN 1674-1056
http://cpb.iphy.ac.cn
http://iopscience.iop.org/cpb
中国物理 B
Chinese Physics
中国物理 Chinese Physics B

Physics of quantum coherence in spin systems

Maimaitiyiming Tusun(麦麦提依明·吐孙), Xing Rong(荣星), Jiangfeng Du(杜江峰)

Citation: Chin. Phys. B . 2019, 28(2): 024204. **doi:** 10.1088/1674-1056/28/2/024204
Journal homepage: http://cpb.iphy.ac.cn; http://iopscience.iop.org/cpb

What follows is a list of articles you may be interested in

Optical coherence transfer over 50-km spooled fiber with frequency instability of 2×10^{-17} at 1 s

Ma Chao-Qun, Wu Li-Fei, Jiang Yan-Yi, Yu Hong-Fu, Bi Zhi-Yi, Ma Long-Sheng
Chin. Phys. B . 2015, 24(8): 084209. **doi:** 10.1088/1674-1056/24/8/084209

Coherence transfer from 1064 nm to 578 nm using an optically referenced frequency comb

Fang Su, Jiang Yan-Yi, Chen Hai-Qin, Yao Yuan, Bi Zhi-Yi, Ma Long-Sheng
Chin. Phys. B . 2015, 24(7): 074202. **doi:** 10.1088/1674-1056/24/7/074202

Multiple frequency conversion via atomic spin coherence of storing a light pulse

Wang Lei, Luo Meng-Xi, Sun Jia-Xiang, Sun Yuan-Hang, Chen Yi, Wei Xiao-Gang, Kang Zhi-Hui, Wang Hai-Hua, Gao Jin-Yue
Chin. Phys. B . 2015, 24(6): 064205. **doi:** 10.1088/1674-1056/24/6/064205

Ghost imaging based on Pearson correlation coefficients

Yu Wen-Kai, Yao Xu-Ri, Liu Xue-Feng, Li Long-Zhen, Zhai Guang-Jie
Chin. Phys. B . 2015, 24(5): 054203. **doi:** 10.1088/1674-1056/24/5/054203

Influence of the illumination coherency and illumination aperture on the ptychographic iterative microscopy

Liu Cheng, Zhu Jian-Qiang, John Rodenburg
Chin. Phys. B . 2015, 24(2): 024201. **doi:** 10.1088/1674-1056/24/2/024201

TOPICAL REVIEW — Fundamental research under high magnetic fields

Physics of quantum coherence in spin systems*

Maimaitiyiming Tusun(麦麦提依明·吐孙)[1,2,3], Xing Rong(荣星)[1,2], and Jiangfeng Du(杜江峰)[1,2,†]

[1] CAS Key Laboratory of Microscale Magnetic Resonance and Department of Modern Physics, University of Science and Technology of China, Hefei 230026, China

[2] Synergetic Innovation Center of Quantum Information and Quantum Physics, University of Science and Technology of China, Hefei 230026, China

[3] School of Physics and Electronic Engineering, Xinjiang Normal University, Urumqi 830054, China

(Received 16 November 2018; revised manuscript received 7 December 2018; published online 25 January 2019)

Quantum computation provides a great speedup over its classical counterpart in solving some hard problems. The advantages of quantum computation come from the coherent superposition principle of quantum mechanics. Spin system is one of the most significant candidates to realize quantum computation. In this review, we focus on the recent experimental progress related to quantum coherence and some fundamental concepts such as the uncertainty principle in the spin systems. We shall first briefly introduce the quantum description of qubit, coherence, and decoherence. Based on this picture, preserving quantum coherence and detection of weak magnetic fields are presented. We also discuss the realization of precise quantum coherent control, adiabatic quantum factorization algorithm, and two aspects of uncertainty relations.

Keywords: coherence, decoherence, magnetic resonance techniques, uncertainty relation

PACS: 42.25.Kb, 03.65.Yz, 87.80.Lg, 03.65.Ta **DOI:** 10.1088/1674-1056/28/2/024204

1. Introduction

The coherent superposition of states combined with the quantification of observable represents one of the most fundamental features of quantum mechanics starting from the classical realm. Through the combination of energy quantization and tensor product structure of the state space, quantum interference, and multiple entanglement phenomena play an important role in the application of quantum physics and quantum information science. Here, we review recently remarkable progress of investigation and exploitation of quantum coherence and its protection based on spin systems, which employ the electron and nuclear spins as spin-qubits.

The present paper is organized as follows. In Section 2, we introduce the concepts of quantum coherence and decoherence. The decoherence we consider is caused by the coupling between the qubit and the environment. We formulate the decoherence as the entanglement between the electron spin and the nuclear spins, which is induced by nuclear spin bath evolution conditioned on the electron spin state. In Section 3, we focus on spin systems. One of the main barriers towards practical quantum computation is the decoherence effect. We utilize dynamical decoupling (DD) techniques to overcome this effect. The dynamical decoupling not only maintains the coherence of single spin qubit, but also preserves the entanglement of multiple qubits. Based on this progress, we demonstrate an anomalous decoherence effect (ADE) of a quantum bath on a spin higher than 1/2. We also discuss the application of quantum coherence in weak magnetic field detection and adiabatic quantum factorization algorithm in the system under study (here is the spin system). In Section 4, we introduce two different uncertainty relation and its experimental verification in the spin systems. The review concludes with Section 5.

2. Coherent spin dynamic

2.1. Coherence and decoherence

A quantum bit (qubit) is a two-level system that can be identified as a spin-1/2 with states $|\uparrow\rangle$ and $|\downarrow\rangle$. The ability of the qubit in a coherent superposition of $|\uparrow\rangle$ and $|\downarrow\rangle$,

$$|\Psi\rangle = \alpha|\uparrow\rangle + \beta|\downarrow\rangle, \tag{1}$$

enables the parallel processing of many pieces of classical information. In order to keep this information, the qubit has to faithfully maintain its quantum state. The unavoidable coupling between the qubit and the environment spoils the quantum state by introducing uncontrolled evolution of the qubit. The qubit coherence is lost under the noisy environment. This decoherence problem is one of the obstacles in the road toward scalable quantum computation.

Let us consider the decoherence problem in the spin system. The system consists of an electron spin qubit and N nuclear spins as the spin bath. The total Hamiltonian can be written as

$$H = H_{\rm e} + H_{\rm n} + H_{\rm en} + H_{\rm nn}, \tag{2}$$

*Project supported by the National Key Research and Development Program of China (Grant Nos. 2018YFA0306600 and 2016YFB0501603), the Fund from the Chinese Academy of Sciences (Grant Nos. GJJSTD20170001, QYZDY-SSW-SLH004, and QYZDB-SSW-SLH005), and the Program from Anhui Initiative in Quantum Information Technologies, China (Grant No. AHY050000).

†Corresponding author. E-mail: djf@ustc.edu.cn

© 2019 Chinese Physical Society and IOP Publishing Ltd

where $H_e = \omega_e S_z$ and $H_n = \Sigma_n \omega_n I_n^z$ are the Zeeman splitting in the applied magnetic field along the z axis, H_{en} is the hyperfine interaction, and H_{nn} is the intrinsic nuclear–nuclear interaction. Suppose the initial state of the qubit-bath system has the form $|\Psi(0)\rangle = |\varphi(0)\rangle \otimes |J\rangle$, which is the direct product of the qubit state $|\varphi(0)\rangle = C_+|\uparrow\rangle + C_-|\downarrow\rangle$ and the bath state $|J\rangle$. After evolution under the Hamiltonian H, for time τ, the nuclear states associated with the two electron spin states diverge, yielding an entangled state of the form

$$\begin{aligned} |\phi(\tau)\rangle &= C_+|\uparrow\rangle \otimes e^{-iH_+\tau}|J\rangle + C_-|\downarrow\rangle \otimes e^{-iH_-\tau}|J\rangle \\ &= C_+|\uparrow\rangle \otimes |J^{(+)}(\tau)\rangle + C_-|\downarrow\rangle \otimes |J^{(-)}(\tau)\rangle. \end{aligned} \quad (3)$$

When the nuclear spin degrees of freedom are traced out, the reduce density matrix becomes

$$\rho(\tau) = \begin{pmatrix} |C_+|^2 & C_+C_-^*\langle J^{(-)}(\tau)|J^{(+)}(\tau)\rangle \\ C_+^*C_-\langle J^{(+)}(\tau)|J^{(-)}(\tau)\rangle & |C_-|^2 \end{pmatrix}. \quad (4)$$

The electron spin coherence is reduced from $\rho_{+-}(0) = C_+C_-^*$ to $\rho_{+-}(\tau) = C_+C_-^*\langle J^{(-)}(\tau)|J^{(+)}(\tau)\rangle$. The decoherence is characterized by

$$L_J(\tau) = \langle J^{(-)}(\tau)|J^{(+)}(\tau)\rangle. \quad (5)$$

This formula simplifies the electron spin coherence to the overlap of the two nuclear states, each following the evolution conditioned on the state of the electron. Thus, the key is the many-body bath dynamics caused by the interaction within the bath. For example, a non-interacting nuclear spin bath would not evolve from an Overhauser field eigenstate (except for a trivial phase factor) and the qubit decoherence would be totally eliminated[1] by standard spin echo.[2]

2.2. Coherence protection

Since qubit decoherence results from uncontrolled evolution due to the coupling between the qubit and the bath, the coherence can be protected by dynamically eliminating the qubit–bath coupling during the evolution. The idea of dynamical decoupling originated in spin echo[2,3] in nuclear magnetic resonance, in which a single flip of nuclear spins by a radio frequency (RF) pulse at least partially cancels the noise. The standard periodic Carr–Purcell–Meiboom–Gill (CPMG) pulse sequences[3] can keep the spin coherence longer by decoupling a spin from its environment.[4] Iteratively concatenated sequences[5–8] can realize the dynamical decoupling to an arbitrarily high order of precision, but the number of pulses increases exponentially with the controlling order. A remarkable advance in dynamical decoupling theory is the discovery by Uhrig[9,10] of optimal sequences, which realizes the Nth order of dynamical decoupling precision with the minimum number (N) of spin-flip pulses. For a pure dephasing model, the sequence of Uhrig dynamical decoupling (UDD) contains N π pulses applied at

$$t_j = t\sin^2\frac{j\pi}{2(N+1)}, \quad j = 1,2,\ldots,N. \quad (6)$$

For comparison, the periodic multiple π pulses sequence called PDD[11] has timing $t_j = t\,(2j-1)/(2N)$. The sequences of UDD and PDD are shown in Fig. 1(a). The experimental preservation of electron spin coherence with dynamical decoupling has been investigated in γ-irradiated malonic acid single crystals.[12] The γ-irradiation may remove one hydrogen atom from a methylene group ($-CH_2$) and create a radical ($-CH$), which provides an unpaired carbon valence electron. The coherence decay of the unpaired-electron spin is investigated both under UDD and PDD. Figure 1(b) shows the experimental results of the coherence decay under N-pulse UDD and PDD, with $N = 1,2,\ldots,7$. It is shown that UDD outperforms PDD in preserving the spin coherence. The coherence time is prolonged to about 30 μs with UDD. It would otherwise be about 0.04 μs without control or 6.2 μs under one-pulse control.

Dynamical decoupling can be utilized to preserve the pseudoentanglement.[13] The experiment was implemented on the system of phosphorus doped in silicon, which is an attractive candidate for spin-based quantum computing. Because the dephasing time of the electron spin (denoted by T_{2e}^* hereafter, $T_{2e}^* = 0.2$ μs) is much shorter than that of the nuclear spin (denoted by T_{2n}^* hereafter, $T_{2n}^* = 30$ μs), it is sufficient to only apply the DD sequence to the electron spin to preserve the pseudoentanglement on a much longer timescale. The degree of pseoduentanglement is quantified by the concurrence C.[14] Figure 2(b) shows the concurrence decay when PDD2 is applied to the electron spin. The decay rate is greatly suppressed compared to that without dynamical decoupling (Fig. 2(a)). The concurrence decay with PDD2 can be well fitted by $C = A_2\exp[-t/T_{\text{decay1}} - (t/T_{\text{decay2}})^3]$, where $T_{\text{decay1}} = 27.673$ μs, and $T_{\text{decay2}} = 23.554$ μs for $|\Phi\rangle = (|\uparrow\downarrow\rangle + |\downarrow\uparrow\rangle)/\sqrt{2}$, and $T_{\text{decay1}} = 30.051$ μs, and $T_{\text{decay2}} = 22.357$ μs for $|\Psi\rangle = (|\uparrow\uparrow\rangle + |\downarrow\downarrow\rangle)/\sqrt{2}$. The cubic exponential term with T_{decay2} is caused by the electron spin decoherence due to spin diffusion of the ^{29}Si spin bath.[15] The linear exponential term with T_{decay1} is caused by both the nuclear spin dephasing and the electron spin decoherence [16]. Since T_{decay1} is comparable with the nuclear spin dephasing time T_{2n}^* but smaller than the electron spin decoherence time $T_{2e} = 60$ μs measured with the Hahn echo sequence, T_{decay1} is mainly limited by the nuclear spin dephasing. To preserve the pseudoentangled states even longer, the suppression of the nuclear spin dephasing is also needed. In this experiment, although the DD sequence is applied only to the electron spin, the lifetime of the pseudoentangled states is extended and is about two orders of magnitude longer than that without dynamical decoupling. Besides, DD can also be used to protect quantum correlations including quantum discord.[17,18]

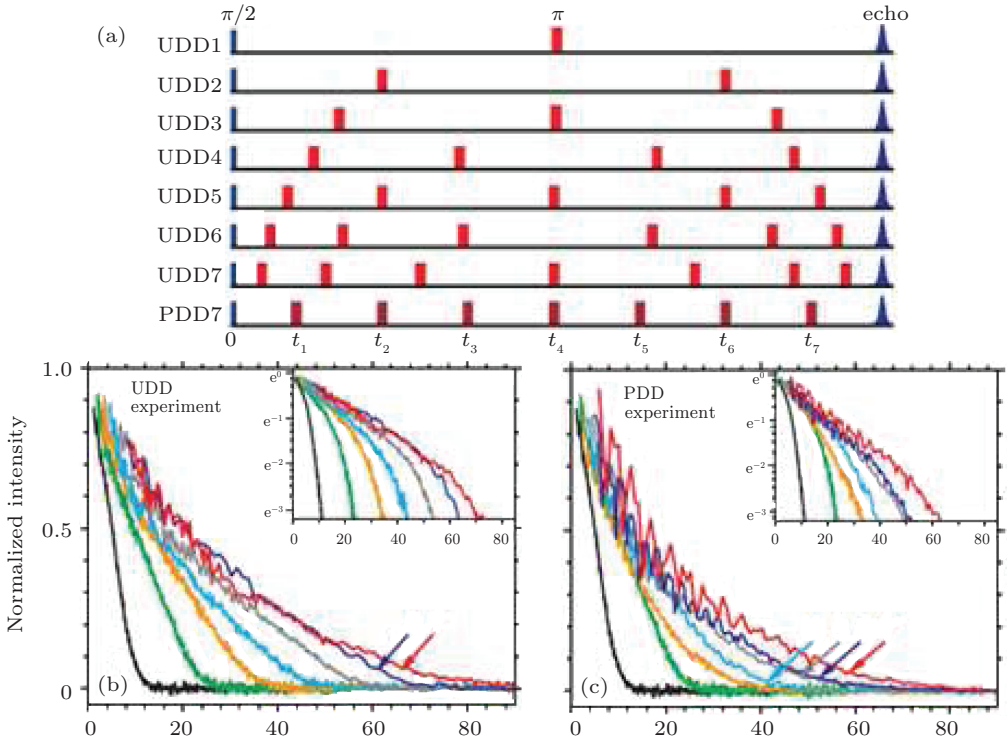


Fig. 1. Experimental preservation of electron spin coherence with dynamical decoupling. (a) Pulse sequences of UDD and PDD when $N = 1, 2, \ldots, 7$. The N-pulse UDD and PDD are abbreviated as UDDN and PDDN, respectively. (b) Experimental results of the coherence decay under UDD (left panel) and PDD (right panel). The integer associated with each curve indicates the number N of π pulses. Insets: semi-logarithmic plots of the same data. Adapted from Ref. [12]. Copyright 2009 by the Nature Publishing Group.

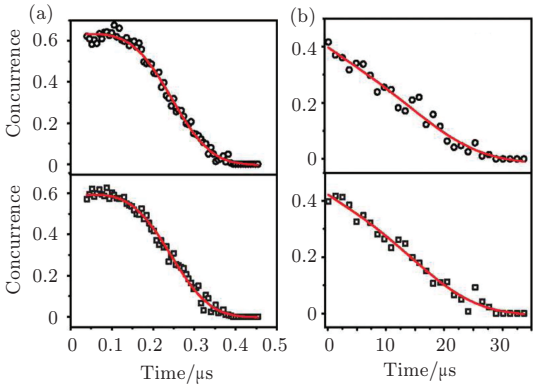


Fig. 2. Experimental preservation of entanglement with PDD2. (a) Decay of concurrence without dynamical decoupling for initial state $|\Phi\rangle$ (upper panel) and $|\Psi\rangle$ (lower panel). (b) Decay of concurrence with PDD2 for initial state $|\Phi\rangle$ (upper panel) and $|\Psi\rangle$ (lower panel). Symbols are the experimental results and solid lines are the fitting results. Adapted from Ref. [13]. Copyright 2011 by the American Physical Society.

The decoherence is caused by the coupling between a quantum object and its environment. Such coupling is usually understood in terms of classical noise, such as in the spectral diffusion theories that are widely used in, for example, magnetic resonance spectroscopy[19,20] and optical spectroscopy.[21,22] A recent theoretical study[23] predicted an anomalous decoherence effect of a quantum bath on a spin higher than 1/2. Considering a spin-1 under a unidirectional magnetic noise b_z with Hamiltonian $b_z S_z$, the spin, initially in a superposition of the S_z eigenstates $|\Psi(0)\rangle = a_-|-\rangle + a_0|0\rangle + a_+|+\rangle$, will evolve to $|\Psi(t)\rangle = a_- e^{i\varphi(t)}|-\rangle + a_0|0\rangle + a_+ e^{i\varphi(t)}|+\rangle$ with an accumulated random phase $\varphi(t) = \int_0^t b(\tau)d\tau$. The coherence of the single-transitions $|0\rangle \leftrightarrow |\pm\rangle$ is determined by the average of the random phase factor as $L_{0,\pm} = \langle e^{\pm i\varphi(t)}\rangle$, whereas the double-transition has coherence $L_{-,+} = \langle e^{2i\varphi(t)}\rangle$. For Gaussian noise, as commonly encountered, $L_{0,\pm} = e^{-\langle\varphi(t)\varphi(t)\rangle/2}$ and $L_{-,+} = e^{-2\langle\varphi(t)\varphi(t)\rangle}$. This leads to the scaling relation

$$L_{-,+} = L_{0,+}^4. \tag{7}$$

Decoherence of the double-transition behaves essentially the same as that of the single-transitions, but is faster as the double-transition suffers from noise that is twice as strong as that suffered by the single-transitions. Surprisingly, in a mesoscopic quantum bath made of nuclear spins, where the noise b_z is the bath operator, the prediction is that the coherence time of the double-transition under dynamical decoupling, where the bath evolution is controlled through the flips of the central spin, can be increased above that of the single spin.[23]

The ADE has been experimentally observed using a nitrogen-vacancy (NV) center system at room temperature.[24] The system consists of center spin and the surrounding ^{13}C nuclear spin has a Hamiltonian $H = H_{\rm NV} + H_{\rm B} + H_{\rm hf}$. The center spin Hamiltonian is $H_{\rm NV} = \Delta S_z^2 - \gamma_e B S_z$, where Δ denotes the zero-field splitting and $\gamma_e = 1.76 \times 10^{11}$ s$^{-1}\cdot$T^{-1} or 2.803 MHz/Gs (The unit 1 Gs $= 10^{-4}$ T) is the electron gyromagnetic ratio. The bath Hamiltonian $H_{\rm B} = \sum_i \omega I_i^z + \sum_{i,j} I_i \cdot \overleftrightarrow{D}_{ij} \cdot I_j$ contains the nuclear spin Zeeman splitting ω and the dipolar interaction between nuclear spins (with coefficients $\overleftrightarrow{D}_{ij}$). The center spin couples to the nuclear spins through

$H_{\rm hf} = S_z \sum_j A_j \cdot I_j \equiv S_z \hat{b}_z$, where A_j is the hyperfine coupling to the j-th nuclear spin I_j. Here, the transverse components of the hyperfine coupling have been dropped because they are too weak to cause the center spin flip (with $A_j \ll \Delta$).

Under a weak magnetic field, the center spin decoherence is mainly induced by the single ^{13}C nuclear spin dynamics.[25–27] The dipolar interaction between nuclear spins can be neglected for the moment. Thus, the bath Hamiltonian $H_{\rm B}$ only contains the nuclear Zeeman energy (with $\gamma_C B/2\pi \sim 14.4$ kHz, $\gamma_C = 6.73 \times 10^7$ s$^{-1}\cdot$T^{-1} being the gyromagnetic ratio of ^{13}C nuclei). The hyperfine field αA_j (with $A_j/2\pi \sim 5$ kHz for a nuclear spin I_j located 1.5 nm from the center) is comparable to the Zeeman frequency. Each nuclear spin precesses about different local fields $h_j^{(\alpha)} = -\gamma_C B + \alpha A_j$, conditioned on the center spin state $|\alpha\rangle$. The center spin decoherence is expressed as[25–27]

$$L_{\alpha,\alpha'}(t) \approx \prod_j \langle I_j^{(\alpha)}(t) | I_j^{(\alpha')}(t) \rangle, \tag{8}$$

where $|I_j^{(\alpha)}(t)\rangle$ is the precession of the j-th nuclear spin about the local field $h_j^{(\alpha)}$ starting from a randomly set initial state $|I_j\rangle$. The conditional evolution of bath spins records the which-way information of the center spin and causes the decoherence. Under a flip operation of the center spin $|\alpha\rangle \leftrightarrow |\alpha'\rangle$, the nuclear spin precession is manipulated as $|I_j^{(\alpha)}(t)\rangle = \exp[-{\rm i}h_j^{(\alpha)} \cdot I(t-\tau)] \exp[-{\rm i}h_j^{(\alpha')} \cdot I_j \tau] |I_j\rangle$, that is, the nuclear spin changes its precession direction and frequency. Thus, the nuclear spin bath is manipulated through control of the center spin. The coherence at the echo time is calculated as[25]

$$L_{\alpha,\alpha'}(2\tau) = \prod_j \left(1 - 2 \left| \sin \frac{h_j^{(\alpha)} \tau}{2} \times \sin \frac{h_j^{(\alpha)} \tau}{2} \right|^2 \right). \tag{9}$$

Figure 3 compares the single- and double-transition coherence under the periodic dynamical decoupling (PDD) control by equally spaced sequences of up to five pulses (applied at τ, 3τ , 5τ,..., called Carr–Purcell sequences for two or more pulses).[28–30]

In the Hahn echo (PDD-1), where the short time condition approximately holds, the single-transition coherence and the double-transition coherence approximately satisfy the scaling relation in Eq. (7). As the number of control pulses increases, the double-transition coherence time increases more than that of the single-transition. Surprisingly, under the five-pulse control, the double-transition has significantly longer coherence time than the single-transition. Such counter-intuitive phenomena unambiguously demonstrate the quantum nature of the nuclear spin bath. All the work indicates that the ADE is robust against the details of the decoherence mechanisms but it is a universal phenomenon due to the quantum nature of mesoscopic baths.

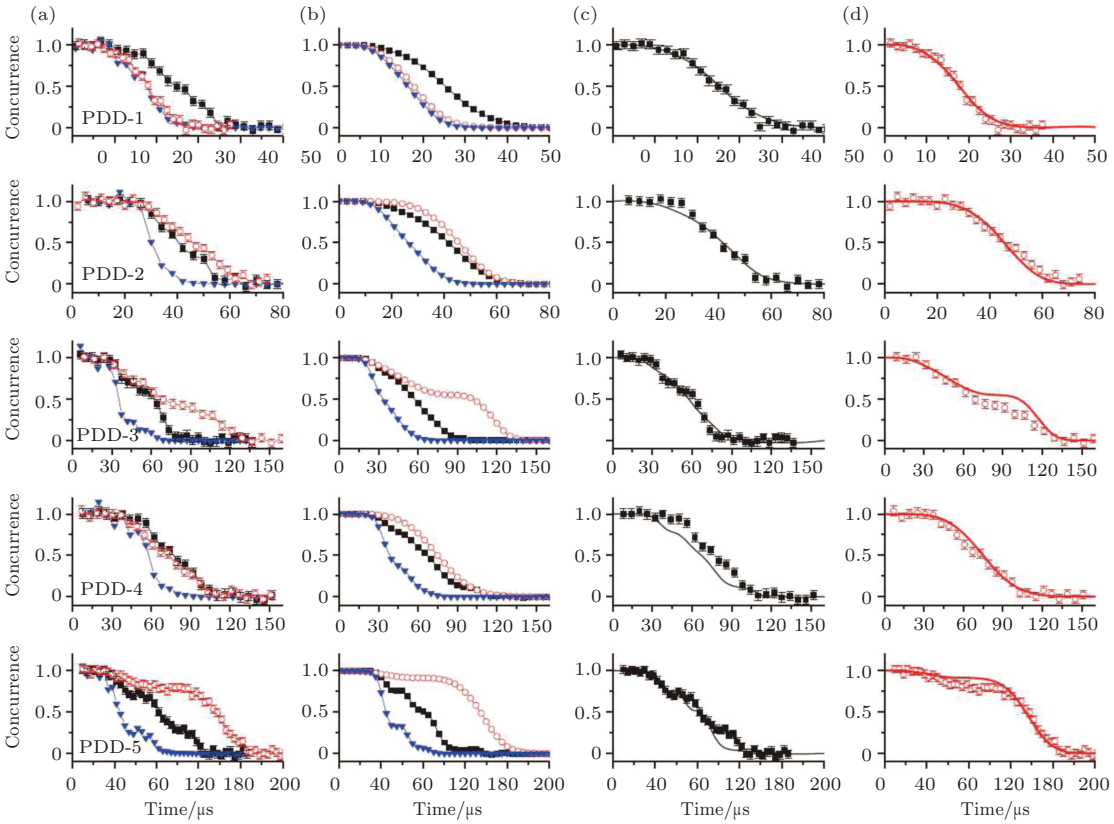


Fig. 3. (a) Measured single- (black line with square symbols) and double-transition coherence (red line with circle symbols), under the one- to five-pulse PDD control (PDD-1 to PDD-5, from top to bottom). The scaled single-transition coherence $L_{0,+}^4$ (blue line with triangle symbols) is plotted for comparison. (b) The calculated data, plotted in the same format as in panel (a). (c) Comparison between the measured (symbols) and the calculated (solid lines) single-transition coherence. (d) The same as panel (c), but for the double-transition. Adapted from Ref. [24]. ©2011 by the Nature Publishing Group.

2.3. Applications of coherence in magnetometery

The detection of weak magnetic fields with high spatial resolution is an important problem in diverse areas ranging from fundamental physics and material science to data storage and biomedical science. An approach to the detection of weak magnetic fields has been developed that takes the advantage of techniques for the coherent control of solid-state electron spin qubits.[31] Specifically, we investigate a magnetic sensor based on nitrogen-vacancy centers in diamond at room temperature. The NV center is a point defect in the diamond lattice, consisting of a nearest-neighboring nitrogen atom substituted for a carbon atom, and a lattice vacancy as illustrated in Fig. 4. The diamond lattice consists of covalently bonded carbon atoms. Each of the four valence electrons of the sp^3-hybridized carbon participates in bonds to the neighboring atoms (distance 1.44 Å). The diamond unit cell is in the $Fd\bar{3}m$ space group, which follows the face-centered cubic Bravais lattice (lattice constant 3.57 Å). In the NV^- center, six electrons occupy the dangling bonds of the vacancy complex, and he resultant defect has C_{3v} point symmetry.[32,33]

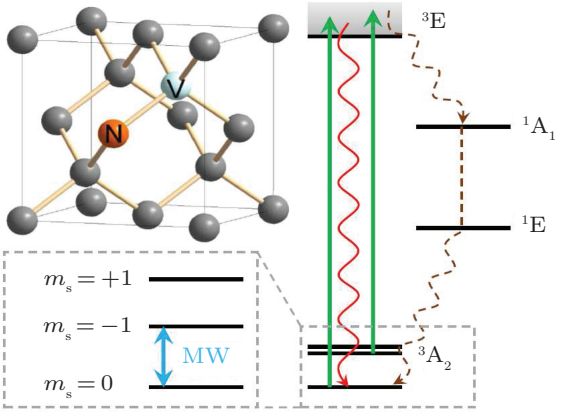


Fig. 4. Negatively charged NV center in diamond and the electronic energy level structure. Adapted from Ref. [34]. ©2017 by the American Physical Society.

The NV system is described by the Hamiltonian as

$$H_{\mathrm{NV}} = \Delta S_z^2 - \gamma_e \boldsymbol{B}\cdot\boldsymbol{S} + \boldsymbol{S}\cdot\overleftrightarrow{\boldsymbol{A}}\cdot\boldsymbol{I}_{\mathrm{N}} + \Delta_{\mathrm{N}}(I_{\mathrm{N}}^z)^2 + \gamma_{\mathrm{N}}\boldsymbol{B}\cdot\boldsymbol{I}_{\mathrm{N}}. \tag{10}$$

Here, Δ is the crystal field splitting along [111] axis which is equal to 2.87 GHz, $\overleftrightarrow{\boldsymbol{A}}$ is the hyperfine coupling between the electron spin and the nearby nitrogen nuclear spin, and the strength of hyperfine coupling is about 2.2 MHz (^{14}N) or 3.1 MHz (^{15}N), and $\Delta_{\mathrm{N}} = 4.95$ MHz is quadrupolar coupling of ^{14}N and it equals 0 for ^{15}N. The external magnetic field leads to Zeeman splitting term in Eq. (10) of NV electron spin $\gamma_e\boldsymbol{B}\cdot\boldsymbol{S}$, and nitrogen nuclear spin $\gamma_{\mathrm{N}}\boldsymbol{B}\cdot\boldsymbol{I}_{\mathrm{N}}$, where γ_e is the electron gyromagnetic ratio for the NV electron spin as given in Subsection 2.2, $\gamma_{\mathrm{N}} = 0.30766$ kHz/Gs for ^{14}N and $\gamma_{\mathrm{N}} = 0.43156$ kHz/Gs for ^{15}N.

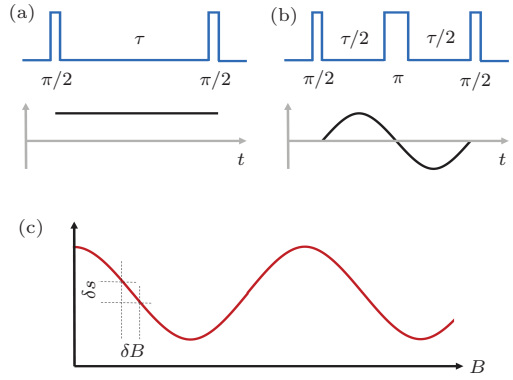


Fig. 5. Protocols to measure DC and AC magnetic field. (a) Ramsey-type sequence applied to detect DC magnetic field. (b) Hahn-echo sequence applied to detect AC magnetic field. (c) Signal *s versus* magnetic field *B*.

A Ramsey-type sequence can be applied to detect a Zeeman shift caused by external magnetic field $\boldsymbol{B}$, as shown in Fig. 5(a). A $\pi/2$ pulse creates a quantum superposition state of $|0\rangle$ and $|1\rangle$. The superposition state $(|0\rangle+|1\rangle)/\sqrt{2}$ will accumulate a phase $\phi = (g\mu_{\mathrm{B}}/\hbar)B\tau$ during the free evolution time τ (here, $\boldsymbol{B}$ is external magnetic field, g is Landé factor of spin, and μ_{B} is Bohr magneton). After the second $\pi/2$ pulse, the population left on $|0\rangle$ state is $s = (1+\cos(2\phi(B)))/2$. In every measurement, deviation $\sigma_s \sim 1/\sqrt{\eta_{\mathrm{d}}c}$ occurs due to quantum projection noise and photon shot noise, where c is the contrast of Ramsey measurement and η_{d} is collection efficiency about 2%–3%.[35]

The minimum detectable magnetic field of NV magnetometer is $\delta B_{\min} = \sigma_s^N/\mathrm{d}s$ (shown in Fig. 5(c)), where $\sigma_s^N = \sigma_s/\sqrt{N}$ is the standard deviation of measurement after N times average, $\mathrm{d}s \sim g\mu_{\mathrm{B}}\tau$ is the slope of the signal *s versus* magnetic field B and $N = T/\tau$ is the measurement times during the total measurement time T. Thus, the minimum detectable direct current (DC) magnetic field scales according to

$$\delta B_{\mathrm{DC}} \approx \frac{\hbar}{g_e\mu_{\mathrm{B}}C\sqrt{T_2^*T}}, \tag{11}$$

where T_2^* is dephasing time which limits the detection time τ and $C = \sqrt{\eta_{\mathrm{d}}c}$. And magnetic field sensitivity of DC magnetic field is[31]

$$\eta_{\mathrm{DC}} \approx \frac{\hbar}{g_e\mu_{\mathrm{B}}C\sqrt{T_2^*}}. \tag{12}$$

Furthermore, alternating current (AC) magnetic field $B_{\mathrm{AC}}(t) = b_{\mathrm{AC}}\sin(\nu t)$ can be measured by matching the sequence $\pi/2 - \tau/2 - \pi - \tau/2 - \pi/2$ with the AC oscillating frequency (Fig. 5(b)). The Hahn echo sequence removes the slow environment noise at the same time. The phase accumulated during the free evolution time is

$$\begin{aligned}\phi &= \int_0^{\tau/2}(g_e\mu_{\mathrm{B}}/\hbar)B_{\mathrm{AC}}(t)\mathrm{d}t - \int_{\tau/2}^{\tau}(g_e\mu_{\mathrm{B}}/\hbar)B_{\mathrm{AC}}(t)\mathrm{d}t \\ &= 2\int_0^{\tau/2}(g_e\mu_{\mathrm{B}}/\hbar)B_{\mathrm{AC}}(t)\mathrm{d}t = 2b_{\mathrm{AC}}\tau/\pi,\end{aligned}$$

where during the second $\tau/2$ free evolution time the spin flips. Sensitivity of AC magnetic field is[31]

$$\eta_{\mathrm{AC}} \approx \frac{\pi\hbar}{2g_e\mu_{\mathrm{B}}C\sqrt{T_2}}. \tag{13}$$

The sensitivity of AC magnetic field can be improve furthermore by higher order dynamical decoupling sequence by extending the decoherence time. The magnetometer sensitivity achieved was 0.5 ± 0.1 $\mu\mathrm{T}\cdot\mathrm{Hz}^{-1/2}$ in Ref. [36] and even 4 $\mathrm{nT}\cdot\mathrm{Hz}^{-1/2}$ in Ref. [37].

NV-based nano-scale nuclear magnetic resonance (NMR) gives a unique opportunity to realize non-destructive and no-labeled structure characterization. In 2011, the theoretical possibility for atomic-scale NV magnetometry of nuclear spin clusters inside and outside diamond was proposed.[26] Later, distant single nuclear spins and several weakly coupled nuclear spins inside diamond were detected[38–41] by dynamical decoupling methods. And in 2013, another method to detect single nuclear spin was demonstrated[42] by continuous microwave (MW) Hartmann–Hahn method. Based on these two methods respectively, the authors in Refs. [43] and [44] proposed single molecule NMR schemes by NV magnetometry aimed in applications in single-molecule spectroscopy in chemistry and biology. Equipped with shallow NV created through ion implantation[45] and δ-doped chemical vapor deposition (CVD) technology,[46] NV magnetometry can be applied to external nuclear spins. The detection of ^{1}H, ^{13}C, or ^{29}Si nuclear spins in various liquid and solid samples has been shown in Refs. [47]– [51] on the diamond surface. This is a key milestone toward achieving nano-scale magnetic resonance imaging based on scanning NV centers. The technique additionally allows one to perform NMR on an arbitrary sample in the regime of ultra-weak and zero magnetic field, because it is based on statistical rather than thermal polarization of the nuclei.

The interactions between nuclear spins can also be investigated with NV center under dynamical decoupling control. A nuclear-dimer induced modulation on the NV center spin coherence can be observed thus both the interactions within the dimer and between the dimer and the NV center electron spin can be characterized.[52] The Hamiltonian of the NV center electron spin and the ^{13}C nuclear spin dimer is[26,27]

$$H = \Delta S_z^2 - \gamma_e \boldsymbol{B}\cdot\boldsymbol{S} + \boldsymbol{S}\cdot\sum_{i=1,2} A_i\cdot\boldsymbol{I}_i + \boldsymbol{I}_1\cdot\mathfrak{D}_{12}\cdot\boldsymbol{I}_2 + \omega_C(I_{1,z}+I_{2,z}). \tag{14}$$

In the strong magnetic field, the dimer dynamics can be described by a pseudo-spin model, where the two-spin states $|\uparrow\downarrow\rangle$ and $|\downarrow\uparrow\rangle$ of the dimer are mapped to the spin-up $|\Uparrow\rangle$ and spin-down $|\Downarrow\rangle$ states of the pseudo-spin σ. The dynamics of the pseudo-spin is governed by the Hamiltonian

$$H_{\mathrm{ps}}^{(m_s)} = \frac{1}{2}\boldsymbol{h}^{(m_s)}\cdot\boldsymbol{\sigma} = \frac{1}{2}(X\sigma_x + Z^{(m_s)}\sigma_z), \tag{15}$$

where the component X is the nuclear spin flip–flop rate due to the inter-nuclear spin dipolar coupling $\mathfrak{D}_{12}$ and the component $Z^{(m_s)}$ is due to the hyperfine couplings difference of the two nuclei induced by the nitrogen-vacancy center electron spin state $|m_s\rangle$. Correspondingly, the pseudo-spin will precess with frequencies $\omega_{\mathrm{ps}}^{(0)} = X$ or $\omega_{\mathrm{ps}}^{(1)} = \sqrt{X^2+[Z^{(1)}]^2}$. When the nitrogen-vacancy center spin is prepared in a superposition state $(|m_s=0\rangle + |m_s=1\rangle)/\sqrt{2}$, the characteristic frequency of the noise induced by the pseudo-spin becomes $\omega_{\mathrm{ps}}^{\mathrm{eff}} = \sqrt{X^2+[Z^{(1)}/2]^2}$. In our experiment, the pseudo-spin precession frequency $\omega_{\mathrm{ps}}^{\mathrm{eff}}$ was measured by dynamical decoupling control[12,28,29] of the nitrogen-vacancy center spin (as shown in Fig. 6).

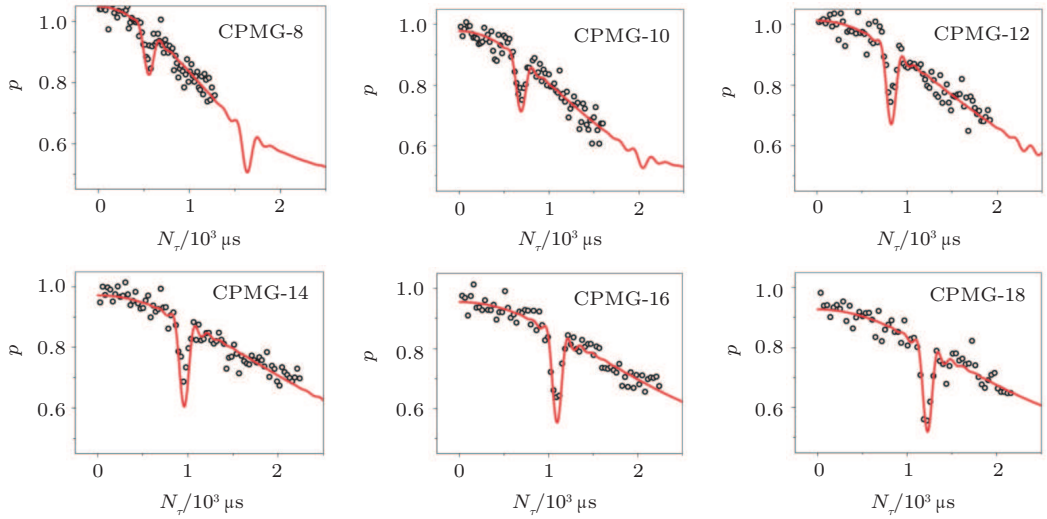


Fig. 6. Characterizing the interaction of a nuclear-spin dimer by fingerprint-matching between measurement and simulation. Nitrogen-vacancy spin coherence as a function of total evolution time under CPMG dynamical decoupling control with various numbers of pulses ($N = 8$, 10, 12, 14, 16, and 18). The experimental data (symbols) are well reproduced by simulations (lines) based on a dimer with interaction $[X, Z^{(m_s)}] = [0.685, 14.6]$ kHz. Other nuclear-spin pairs do not produce dip features matching the experimental data. In these measurements, the magnetic field is $B_0 = 1770$ Gs. The vertical axes show the probability in the $|0\rangle$ state. Adapted from Ref. [52]. ©2014 by the Nature Publishing Group.

Besides NV-based nano-scale nuclear magnetic resonance, NV-based single molecule electron spin resonance(ESR) finds broad application for studying basic molecular mechanisms in biology and chemistry.[53] Most proteins, however, are non-paramagnetic, and thus not accessible by the technique. Labeling biomolecules with a small spin-bearing moiety, such as nitroxide spin labels, enables electron spin resonance to acquire a broad range of structural and dynamical information. However, current methods require 10^{10} uniform molecules to accumulate a sufficiently large signal-to-noise ratio. This substantially complicates compiling structural and dynamical information. New methods that have tried to push the sensitivity of magnetic resonance to the single spin level all require either a dedicated environment[54,55] or conducting surfaces and tips.[56]

The NV center's triplet ($S=1$) ground state can be spin-polarized and read out optically. The magnetic dipole interaction between the NV spin and the dark electron spin is conveniently measured by simultaneously driving the probe (NV) and the dark electron spin. Single NV centers can be created roughly 5 nm below the surface of diamond by ion implantation. The dark spin sample can be deposited on diamond surface and characterized by atomic force microscopy (AFM).

Denoting the spins by $S_{\rm NV}$ (NV sensor), $S_{\rm e}$ (dark electron spin), and I (nuclear spin of dark electron spin), the combined system can be modelled by a coupling Hamiltonian

$$H=\overbrace{\Delta S_{z,\rm NV}^2+\gamma_{\rm NV}B_0S_{z,\rm NV}}^{H_{\rm NV}}+\overbrace{b_{\rm e}S_{z,\rm NV}S_{z,\rm e}}^{H_{\rm NV,dark}}+\overbrace{\gamma_{\rm e}B_0S_{z,\rm e}+S_{\rm e}AI+\gamma_I B_0I_z+IQI}^{H_{\rm dark}},\tag{16}$$

where dark denotes the dark electron spin, B_0 is the external static field (aligned along z), Δ is the zero-field splitting of the NV, Q is the nuclear quadrupole coupling constant, and $\gamma_{\rm NV}$, $\gamma_{\rm e}$, and γ_I are the gyromagnetic ratios of the NV, target electron, and nuclear spin, respectively. The coupling between the NV and the dark electron spin is approximated as a pure $S_{z,\rm NV}-S_{z,\rm e}$ interaction with a coupling constant $b_{\rm e}$, because it is much smaller than the Zeeman and zero-field splitting of the two spins. Within this approximation, the target spin generates an effective magnetic field $B_{\rm e}=b_{\rm e}S_{z,\rm e}/\gamma_{\rm NV}$ at the NV center site, which depends on the quantum number $S_{z,\rm e}$.

To reveal the coupling, two protocols of spin-echo detected the double electron–electron resonance (known as SEDOR or DEER[48,57–59]). In both schemes, the effective two-level system $|0\rangle=|S_z=0\rangle, |1\rangle=|S_z=-1\rangle$ of the NV spin S is addressed with a resonant microwave and performs a Hahn-echo measurement on this system. In this measurement, an initial $\pi/2$ pulse prepares the spin in a coherent superposition $|\psi(t=0)\rangle=(|0\rangle+e^{i\varphi}|1\rangle)/\sqrt{2}$ with $\varphi=0$. φ evolves over time, and is refocused by the π pulse at $t=\tau$ and converted into population by the final $\pi/2$ pulse, so that the result of a subsequent measurement is $|\langle 0|\psi\rangle|^2=(1+C(\tau)\cos(\varphi(2\tau)))$.

Here,

$$\varphi(2\tau)=\mu_S\Big(\int_0^{\tau}{\rm d}tB(t)-\int_{\tau}^{2\tau}{\rm d}tB(t)\Big),\tag{17}$$

where the sign "−" accounts for the refocusing π pulse. $C(\tau)\le 1$ is a factor accounting for a possible loss of coherence.

A modified version of SEDOR can enhance sensitivity of single spin ESR protocols. The pulse sequence is shown in Fig. 7(a). The phase φ evolves over time, is refocused by N π-pulses at $t=\tau_0/2+n\tau_0$, and is converted into a population by the final $\pi/2$ pulse at $t=N\tau_0$. The key idea is to map the electron spin resonance signal of the spin label $S_{\rm e}$ to a phase φ on the NV spin. The flip π pulses of NV electron spin and dark electron spin are synchronized with the dynamical decoupling period. The NV experiences an alternating field from the dark electron spin label and acquires a phase

$$\varphi\sim b_{\rm eff}N\tau_0,\tag{18}$$

where $b_{\rm eff}$ is the effective magnetic field generated by the spin label at the location of the NV spin. In this way, the dark electron spin ESR signal is mapped to the signal obtained from the NV sensor.

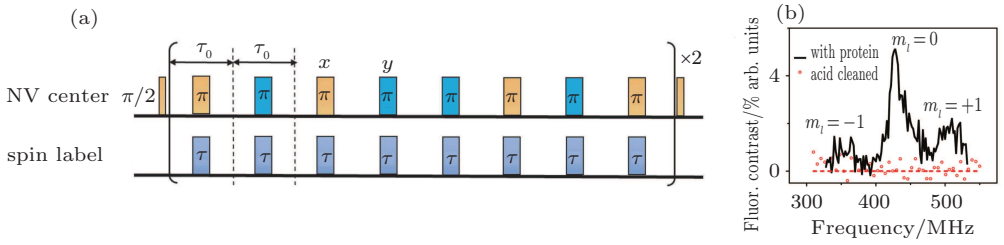


Fig. 7. Experimental pulse sequence and electron spin resonance spectrum of dark spin. (a) Pulse sequence to measure the coupling of an NV sensor to the dark electron spin. The pulse sequences contain MW and RF channels, in which microwave and radio-frequency pulses are used to control the NV probe and synchronously flip the dark electron spin. (b) Single spin ESR spectra under ambient conditions. The spectrum disappears after removing the protein by acid cleaning. Adapted from Ref. [60]. ©2015 by the American Association for the Advancement of Science.

Figure 7(b) shows the ESR spectrum of a single dark spin (a spin label on protein) under ambient environment. Upon cleaning the diamond surface, the signal disappears, demonstrating that it stems from the spin label on the protein. The spectra in Fig. 7(b) are recorded at an external magnetic field $B_0 = 153.0$ Gs. Three spectral peaks at 356.3 MHz, 430.9 MHz, and 501.6 MHz, mark the hyperfine splitting between the spin label electron spin ($S = 1/2$) and the nitrogen nuclear spin ($I = 1$). The observation of hyperfine splitting proves that the detected spin is indeed the nitroxide spin on the protein and not, *e.g.*, that of a substitutional nitrogen impurity inside diamond.

3. Coherent spin control

3.1. Coherent spin control in single molecular magnets

Quantum computation requires not only quantum state with long coherent time but also precise coherent quantum control. Single molecular magnets (SMMs) are among the potential systems for quantum memory[61] and quantum information processing.[62] Quantum coherence and oscillation are critical for these applications. The ground-state quantum coherence and Rabi oscillations of the SMM V_{15} ($[V_{15}^{num4}As_6^{num3}O_{42}(H_2O)]^{6-}$)[63] have been observed at 2.4 K together with scrutinized validation.[64] The new signal of the Rabi oscillation of the ground state ($S = 1/2$) is shown in Fig. 8. Relaxation times are recorded to be $T_2 = 187.7 \pm 4.4$ ns for $S = 3/2$ and $T_2 = 149 \pm 10$ ns for $S = 1/2$ with echo decay curves shown in the inset of Fig. 8. The observing of ground-state quantum oscillation is particularly important in further studies of quantum effect in SMMs. The coherence property of V_{15} makes it potentially suitable for qubit implementation, where the coherence time can be improved by, for example, using deuterated surfactants and solvent or applying dynamic decoupling approaches.[12,13]

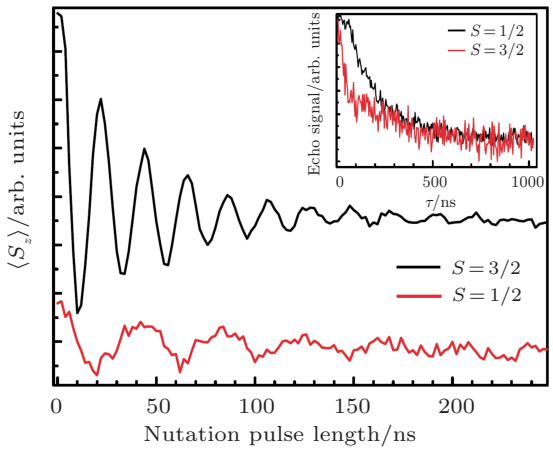


Fig. 8. The time evolution of the average spin $\langle S_z \rangle$ after a spin-echo sequence of $S = 1/2$ states (lower curve) and the $S = 3/2$ states (upper curve). Inset: the T_2 decay curves for $S = 1/2$ (lower curve) and $S = 3/2$ (upper curve) measured with Hahn echo sequences. Adapted from Ref. [64]. ©2012 by the American Physical Society.

3.2. High fidelity coherent spin control

In order to achieve reliable quantum-information processing results, we need to protect quantum gates along with the qubits from decoherence. Among the various approaches to quantum coherence protection, dynamical decoupling[11] is a particularly promising strategy due to its integratability with quantum gates by elaborate designs. Protecting quantum logic tasks with pulsed DD has been reviewed in Section 2 for extending the coherence time of individual qubit and two-qubit entanglement. Despite the great success of pulsed DD in protecting the coherence, it becomes complicated to combine DD sequence with quantum gates when considering the commutation between the decoupling pulses and the control pulses. Continuous-wave dynamical decoupling (CWDD) approaches have been developed to retain the flexibility of carrying out quantum logic tasks while the qubits are protected.[65–69] The combination of CWDD and quantum gates has been presented in a solid-state NV center system in diamond.[70]

The loss of quantum coherence of the NV center is mainly caused by the surrounding ^{13}C nuclear spin bath fluctuations. This can be described by an effective weak random magnetic field b. The linear dependence of the energies $|\pm 1\rangle$ on the magnetic field results in a sharp variation of the energy gap $\omega_{0,-1}$ between the two states of the qubit ($|0\rangle$ and $|-1\rangle$). This results in strong decoherence due to the random magnetic field b. An equally weighted superposition of $|\pm 1\rangle$ can result in states with eigenvalues insensitive to the random field b. This can be realized by applying two off-resonant continuous microwave driving fields to $|0\rangle \rightarrow |\pm 1\rangle$ at the same time by ω_1 and ω_2. The Hamiltonian of the NV center driven by two microwaves of the same off-resonance δ_o and Rabi frequency Ω can be written in the interaction picture as follows:

$$H_{\rm NV} = \sum_{\iota=\pm 1} [(\delta_o + \gamma_e b\iota)|\iota\rangle\langle\iota| + \frac{\Omega}{2}(|0\rangle\langle\iota| + |\iota\rangle\langle 0|)]. \quad (19)$$

The diagonalization of $H_{\rm NV}$ results in three dressed states, $|e\rangle$, $|d\rangle$, and $|g\rangle$ in the driven space. The two lower levels $|d\rangle$ and $|g\rangle$ of the gap w_{dg} are used as a qubit. Owing to the symmetry of $H_{\rm NV}$ and nonzero Ω, the energies of all the three states are only functions of b^2, which are insensitive to b, in contrast to the linear dependence of $\delta\omega_{0,-1}$ on $|b|$. Hence, the dephasing between $|d\rangle$ and $|g\rangle$ will be strongly suppressed when the microwave Rabi frequency Ω is much larger than the weak effective random field. With the appropriate ratio of $\Omega/\delta_o(=4)$, even the b^2 term in w_{dg} is eliminated so that the lowest order is $\sim b^4$, and a much greater coherence time can be achieved in the protected subspace spanned by $|d\rangle$ and $|g\rangle$.[65] The gradual transfer from $|0\rangle$ to $|g\rangle$ when the microwave Rabi frequency Ω gradually increases allows adiabatical preparation and readout, and the manipulation of the dressed state can be realized by an RF pulse.

Figure 9(a) plots the Rabi oscillation in the $M_s = 0, -1$ bases without the driven and $|d\rangle$, $|g\rangle$ bases with CWDD. It clearly shows that the oscillation in $|d\rangle$, $|g\rangle$ is well preserved almost without decay even after 25 μs, while that in the $M_s = 0, -1$ bases suffers considerable decay even in a few μs. The performance of the CWDD-protected quantum gate is evaluated using the coherence of the state after successive NOT gate operations. It is shown in Fig. 9(b) by plotting the indicator F defined to be $|\langle\psi|d\rangle|^2$ for odd numbers of NOT gates and $|\langle\psi|g\rangle|^2$ for even numbers of NOT gates. Compared to the decay time of 11 μs in the undriven case, the coherence of the CWDD-driven case is maintained far beyond 50 μs, clearly demonstrating the performance of the quantum gate protected with CWDD.

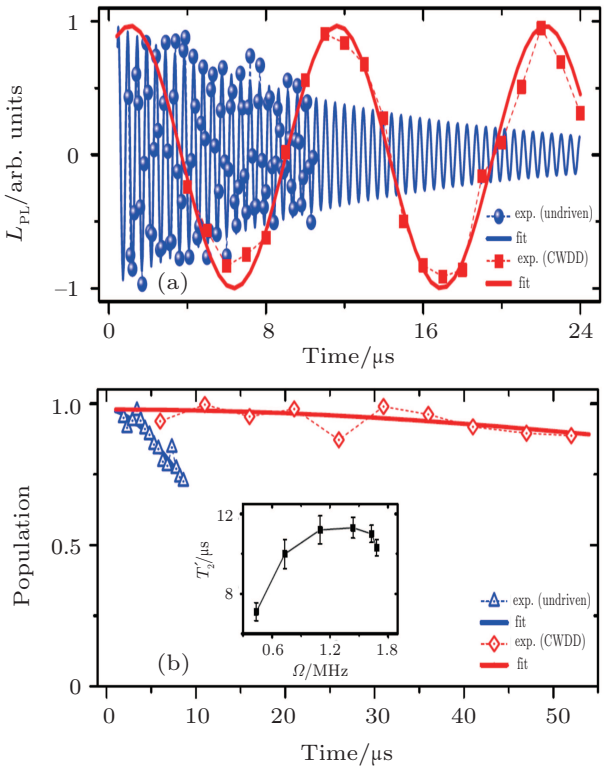


Fig. 9. (a) Measured decay of Rabi oscillation both in the undriven space (spheres) and in the subspace protected by CWDD (squares); the curve is only for guiding the eyes. (b) The population of the designated state as a result of the successive NOT gate operation in undriven space with microwave π pulse (triangles), or in a CWDD-protected space with RF π pulse (diamonds). The curve is fitted to Gauss lineshape decays. The subset is the measured decay time T_2' as a function of the microwave field amplitude Ω. Adapted from Ref. [70]. ©2012 by the American Physical Society.

Except for the DD strategy for protecting quantum control discussed above, theoretical schemes termed dynamical corrected gates (DCGs) have been proposed.[71–75] To illustrate this, let us consider the case of realizing a target single-qubit gate $R_\phi(\theta)$, which denotes the rotation of an angle θ around the axis in the equatorial plane with azimuth ϕ. For simplicity, we consider the on-resonance case ($\Omega = 0$) and set $\phi = 0$. Without considering the qubit-environment coupling, the target gate can be realized by appropriate duration of evolution under the Hamiltonian $H_{\text{ideal}} = 2\pi\omega_1 S_x$, where ω_1 is the strength of the control (microwave) field. Due to the inevitable qubit–environment coupling, the electron-spin qubit is subjected to the Hamiltonian $H_{\text{prac}} = 2\pi(\delta S_z + \omega_1 S_x)$, where δ is the random Overhauser field resulting from the interaction between the electron spin qubit and the nuclear spin bath. The error term δS_z in the Hamiltonian renders the realized gate apart from the target. Due to the nuclear spin flip, the value of δ changes in every new trail of experiment, leading to different gates realized for different trails. When averaging over many trails to set up the statics, we will obtain a non-unitary process on average rather than the target unitary gate.

A type of DCG, named soft uniaxial positive control for orthogonal drift error (SUPCODE),[75] has been experimentally implemented to suppress decoherence during quantum gates to the limit set by $T_{1\rho}$.[76] The SUPCODE is a class of pulse sequences which was originally proposed to suppress the fluctuations in the magnetic field gradient during quantum gates in the system of singlet-triplet spin qubit in a semiconductor double quantum dot.[75] It was soon experimentally demonstrated that SUPCODE can be utilized to suppress the fluctuation of the Overhauser field δ on the electron spin qubit.[76] The N-piece SUPCODE sequence contains N pieces of pulses. With each piece of pulse realizing an evolution operator containing δ, the total N pieces generate the target gate with the error δ suppressed to a certain order. Taking the five-piece SUPCODE as an example, the sequence for a target gate $R_0(\theta)$ is $\tau_1 - R_0(\theta/2) - \tau_3 - R_0(\theta/2) - \tau_1$, where $\tau_1 = \csc\theta(1 - 2\cos(\theta/2) + \cos\theta + \sqrt{4 - 8\cos(\theta/2) + 4\cos\theta + \theta\sin\theta})$ and $\tau_3 = -2(\tau_1\cos(\theta/2) + \sin(\theta/2))$ are waiting times (in unit of $1/(2\pi\omega_1)$) without the control pulse, $\theta \in (2\pi, 3\pi)$. The sequence generates a gate of which the fidelity with the target gate only contains sixth and higher orders of δ/ω_1. Note that the target gates $R_0(\theta)$ when $\theta \in (0, \pi)$ can be realized with the five-piece SUPCODE sequence of $R_0(\theta + 2\pi)$, and $R_0(\pi)$ can be realized by repeating the five-piece SUPCODE sequence of $R_0(2.5\pi)$ twice.

The experiment was implemented on the single electron spin of an NV center in diamond.[77] The NV center consists of a substitutional nitrogen atom with an adjacent vacancy cite in the diamond crystal lattice. As an important candidate for quantum computation,[78] a single NV center provides a spin register composed of an electron spin, a host nitrogen nuclear spin, and several ^{13}C nuclear spins. In this experiment, the states $|m_S = 0\rangle$ and $|m_S = 1\rangle$ of the electron spin are encoded as a qubit. A magnetic field of 513 Gs is applied along the NV symmetry axis ([111] crystal axis) to achieve effective polarization of the nitrogen nuclear spin.[79,80] The undesired couplings between the electron spin and the surrounding ^{13}C nuclear spins lead to the decoherence effect, which should be suppressed during quantum gates to achieve high fidelity.

The SUPCODE sequences are utilized to realize decoherence-protected quantum gates in the experiment. To minimize the influence of the instability of the control field, the control strength is set to $\omega_1 = 1$ MHz. In Fig. 10(a), the quantum oscillation driven by five-piece SUPCODE and that driven by naive pulses are compared. The envelope decay of the oscillations presents loss of coherence during the state evolutions. It is clearly shown that the loss of coherence caused by decoherence effect is greatly suppressed when driving the qubit with five-piece SUPCODE compared to that with naive pulses. The decay time is derived to be $T_{\rm DCG} = 690(40)$ μs for the oscillation driven by five-piece SUPCODE, and $T_2' = 135(10)$ μ s for that driven by naive pulses, from the fitting of the experimental data. As a reference, figure 10(c) shows the coherence time when N-pulse dynamical decoupling is applied. As N increases, the coherence time saturates at $T_{1\rho} = 660(80)$ μs, which is determined by an independent spin-locking experiment. The decay times are summarized in Fig. 10(d). It is noted that $T_{\rm DCG}$ has reached $T_{1\rho}$ within the uncertainty. This indicates that the decoherence effect has been suppressed to the limit set by $T_{1\rho}$ when realizing quantum gates with five-piece SUPCODE. To verify this, the five-piece SUPCODE sequence for $R_0(\pi/2)$ is successively applied and the fidelity[81] decay is recorded using quantum process tomography. As shown in Fig. 10(b), the experimental fidelity decay matches the theoretical prediction in which only the $T_{1\rho}$ process is taken into account. With this method, the fidelity of each five-piece SUPCODE $\pi/2$ gate is derived to be 0.9961(2).

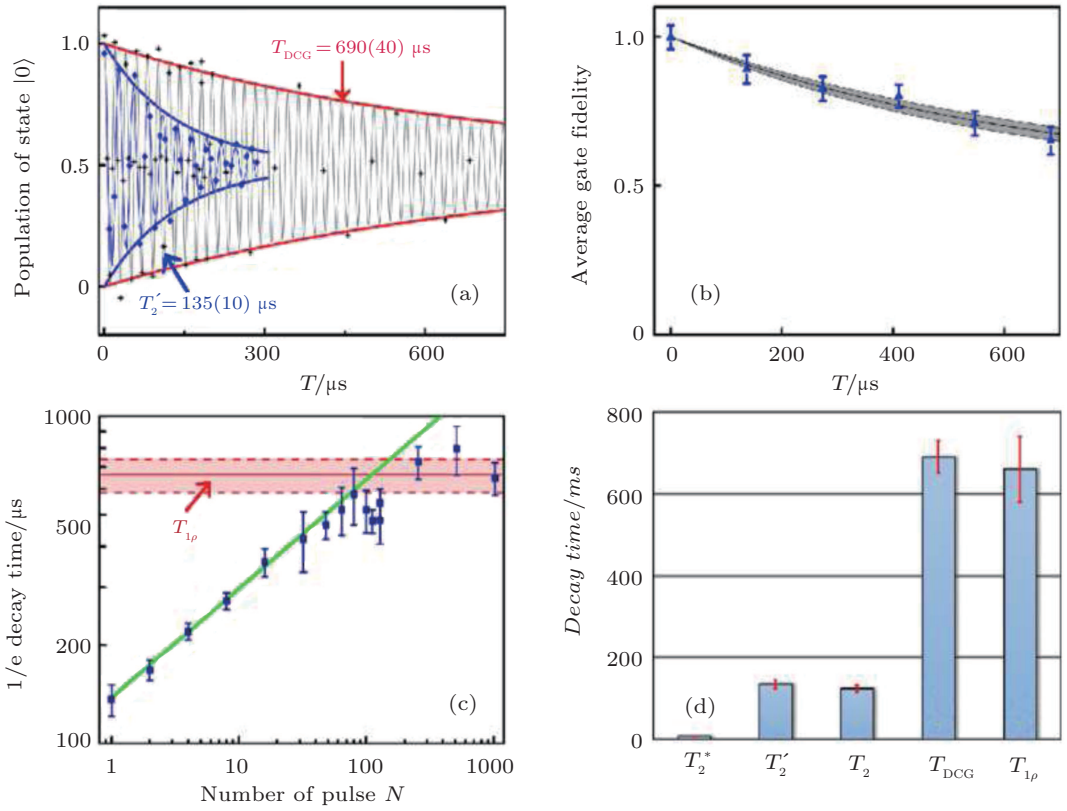


Fig. 10. Experimental suppression of decoherence effect during quantum gates *via* SUPCODE. (a) Comparison of the quantum oscillation driven by five-piece SUPCODE pulses with that driven by naive pulses. Symbols are experimental results and solid lines are the fitting results. (b) Decay of the fidelity of successively applied gates by five-piece SUPCODE. Symbols are experimental results obtained *via* quantum process tomography, and the solid line is the theoretical prediction only considering the $T_{1\rho}$ process. The shaded region is calculated with the uncertainty of the measured $T_{1\rho}$. (c) Extended coherence times *via* N-pulse dynamical decoupling. The coherence time saturates at $T_{1\rho} = 660(80)$ μs for sufficiently large N. (d) Comparison of the decay times. Adapted from Ref. [76]. ©2014 by the American Physical Society.

To further improve the gate fidelity, the instability of the control field[82] as well as the decoherence effect should be simultaneously suppressed during the quantum gates. The SUPCODE pulse can suppress the dephasing effect during the gate operations, but it is sensitive to the error due to the instability of the control field. That is why the control strength is set to $\omega_1 = 1$ MHz in the above experiment to demonstrate the suppression of decoherence to the $T_{1\rho}$ limit.[76] A pulse sequence which is insensitive to the instability of control field is named broadband number 1 (BB1).[83] The BB1 sequence for a target gate $R_0(\theta)$ is $R_0(\theta/2) - R_\phi(\pi) - R_{3\phi}(2\pi) - R_\phi(\pi) - R_0(\theta/2)$, where $\phi = \arccos(-\theta/4\pi)$. To achieve simultaneous suppression of errors due to both decoherence effect and instability of the control field, the concept of concatenated composite[84] pulse may be adopted. A novel concatenated composite pulse named BB1inC has been designed and experimentally imple-

mented on the electron spin of an NV center in diamond.[85] The BB1inC sequence for a target gate $R_0(\theta)$ is $R_0(\theta/2) - R_\phi(\pi) - R_{3\phi}(2\pi) - R_\phi(\pi) - R_0(\theta_3) - R_\pi(\theta_2) - R_0(\theta_1)$, where $\phi = \arccos(-\theta/4\pi)$, $\theta_1 = \theta/2 - \arcsin[\sin(\theta/2)/2]$, $\theta_2 = 2\pi - 2\arcsin[\sin(\theta/2)/2]$, and $\theta_3 = 2\pi - \arcsin[\sin(\theta/2)/2]$. The gate fidelity is experimentally quantified with the standard technique of randomized benchmarking.[86] The experimental results are shown in Fig. 11(a), where the control strength is set to $\omega_1 = 10$ MHz. An average gate fidelity of $F_a = 0.999952(6)$ is achieved for the gates realized with BB1inC.

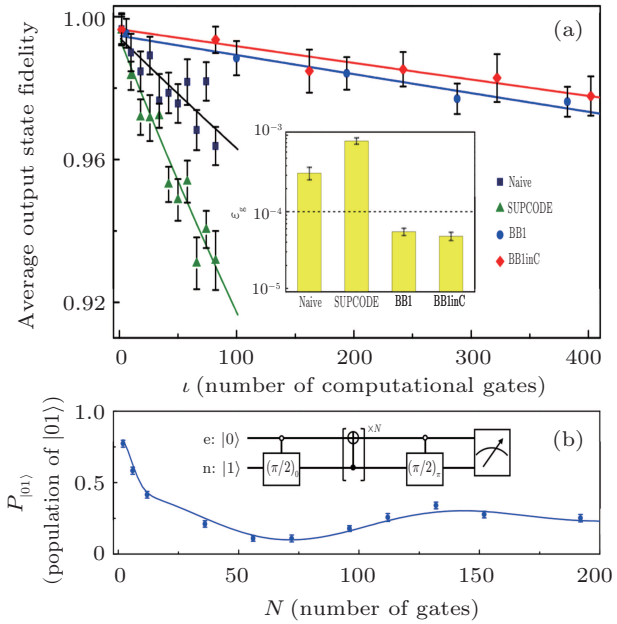


Fig. 11. Experimental results of universal quantum gates with fault-tolerant fidelity on an NV center in diamond. (a) Experimental results of randomized benchmarking for quantifying the average gate fidelity F_a of single-qubit gates on the electron spin qubit of the NV center. Symbols are experimental results and solid lines are the fitting results from which F_a is derived. Inset: comparison of the error per gate $(1 - F_a)$ of naive, SUPCODE, BB1, and BB1inC pulses. (b) Experimental results for measurement of the two-qubit CNOT gate fidelity. Symbols are experimental results and solid lines are the fitting results from which the CNOT gate fidelity is derived. Inset: the measurement sequence. Adapted from Ref. [85]. ©2014 by the Nature Publishing Group

Quantum computation requires a universal set of quantum gates, including not only universal single-qubit gates but also a non-trivial two-qubit gate (*e.g.*, the CNOT gate). The sequence of two-qubit CNOT gate with simultaneous suppression of the errors due to both decoherence effect and the instability of control field can be designed with the optimal control method, especially the technique of gradient ascent pulse engineering (GRAPE).[87] For the hybrid electron-nuclear spin system, since the electron spin qubit is more sensitive to noises than the nuclear spin, it is sufficient to take into account only the noise felt by the electron spin in the optimization process. The sequence for a CNOT gate on the electron and ^{14}N nuclear spins of an NV center has been designed with this method and experimentally implemented.[85] By repeatedly applying the CNOT gate and recording the dynamics of state evolution, the average fidelity of each CNOT gate can be derived. Figure 11(b) shows the experimental results of state population with repeated application of the CNOT gate; the population of state $|01\rangle$, $P_{|01\rangle}$, exhibits oscillatory attenuation as the number of gates increases. The decay of $P_{|01\rangle}$ is mainly owing to the quasi-static fluctuation of δ and the instability of the control field, which are quantitatively characterized with additional experiments. The oscillation is due to the deviation of the practical Hamiltonian from the ideal one under which the evolution generates a CNOT gate. The parameters describing the practical Hamiltonian can be derived by fitting the experimental data. With the practical Hamiltonian as well as the errors due to δ and the instability of the control field characterized quantitatively, the practical evolution and its fidelity with the CNOT gate can be obtained. The gate fidelity is determined to be 0.9920(1). Together with the single-qubit gates realized with BB1inC, a universal set of quantum gates with fault-tolerant fidelity[88] has been demonstrated on the NV center in diamond.

3.3. Time-optimal control

Although high fidelity universal control has been reviewed above, the ultimate goal of quantum control is to achieve high-fidelity universal. The quantum brachistochrone equation (QBE) has been proposed to provide a general framework for finding time-optimal state evolutions or unitary operations.[89–95] The quantum system is considered to be driven by the Hamiltonian $H(t)$, which is described by the Schrödinger equation $\dot{U} = -\mathrm{i}H(t)U$, with boundary conditions $U(0) = I$ and $U(T) = U_F$ (we set $\hbar = 1$). The path with the minimal time cost can be obtained by solving the QBE[90] together with Schrödinger equation. The QBE is written as

$$\dot{F} = -\mathrm{i}[H, F], \tag{20}$$

where $F = \partial L_C/\partial H$ and $L_C = \sum_j \lambda_j f_j(H)$, with λ_j being the Lagrange multiplier. One physically relevant constraint is the finite energy bandwidth described as $f_0(H) \equiv [\mathrm{Tr}(H^2) - E^2]/2 = 0$, where E is a constant. Reference [95] provides a method to obtain the accurate minimum-time protocol by solving the QBE equation. In realistic physical systems, part of the Hamiltonian H is usually time independent (*e.g.*, fixed couplings between spin–qubits), and the reasonable constraint for the energy is actually for the time variable part (*e.g.*, the shaped microwave pulse with bounded power). The original QBE is not able to provide solution to this problem directly. The Hamiltonian can be rewritten as $H(t)$ as $H = H_0 + H_c(t)$, where the drift Hamiltonian H_0 stands for the time invariable part and $H_c(t)$ stands for the control Hamiltonian. The drift Hamiltonian H_0 can be fixed spin couplings or nonzero constant external magnetic field. The control Hamiltonian $H_c(t)$

can be a controllable external magnetic field or adjustable couplings between qubits. The constraint of finite energy bandwidth is modified to $f_0(H_c) = 0$. Then the time-optimal control (TOC) of multiple qubits, which is experimentally feasible, can be obtained by solving the QBE with the mentioned improvements.

The experimental realization of time-optimal universal control has been reported in a two-qubit system, which consists of an electron spin and a nuclear spin of a nitrogen-vacancy center in diamond.[96] The electron (nuclear) spin states $|m_S = 0\rangle$ and $|m_S = -1\rangle$ ($|m_I = 1\rangle$ and $|m_I = 0\rangle$) are encoded as the electron (nuclear) spin qubit. Universal control of a single qubit requires the ability to realize rotations around two different axes of the Bloch sphere. The evolution operator is denoted as $R(\hat{\boldsymbol{n}}, \theta)$, corresponding to a rotation of angle θ around the axis $\hat{\boldsymbol{n}} = \hat{\boldsymbol{x}}\sin\gamma\cos\varphi + \hat{\boldsymbol{y}}\sin\gamma\sin\varphi + \hat{\boldsymbol{z}}\cos\gamma$.

The realization of a target unitary transformation $R(\hat{\boldsymbol{z}}, \pi)$ when $\delta = 0$ is taken as an example to compare the time cost between the derived TOC and a nonoptimized evolution path with Euler rotation: $R(\hat{\boldsymbol{z}}, \theta) = R(\hat{\boldsymbol{x}}, \pi/2)R(\hat{\boldsymbol{y}}, \theta)R(-\hat{\boldsymbol{x}}, \pi/2)$. Figure 12(a) shows the state evolution during $R(\hat{\boldsymbol{z}}, \pi)$. The initial state is prepared to $(|m_s = 0\rangle + \mathrm{i}|m_s = -1\rangle)/\sqrt{2}$. As shown in Fig. 12(a), the target evolution of $R(\hat{\boldsymbol{z}}, \pi)$ is realized at 173.2 ns with TOC and at 200 ns with Euler rotation. The case when $\delta \neq 0$ has also been experimentally implemented. Both $R(\hat{\boldsymbol{z}}, \theta)$ and $R(\hat{\boldsymbol{x}}, \theta)$ with various values of θ have been demonstrated. Furthermore, time-optimal universal single-qubit control with other constraints on H_c is also experimentally demonstrated. The preformance of the gates are characterized utilizing quantum process tomography.[97] All the gate fidelities are measured to be above 0.99. Except for the single qubit gates, a non-trivial two-qubit controlled-U gate

$$U_c = \begin{pmatrix} 1 & 0 & 0 & 0 \\ 0 & 0 & 0 & 1 \\ 0 & 0 & 1 & 0 \\ 0 & -1 & 0 & 0 \end{pmatrix}, \tag{21}$$

is also demonstrated.[96] The TOC Hamiltonian is obtained by numerically solving the QBE together with Schrödinger equation. The time duration of the gate is 446 ns. The performance of the U_c gate is characterized by quantum process tomography as shown in Fig. 12(b). The average gate fidelity of the two-qubit gate is 0.99(1), which reaches the threshold of fault-tolerant quantum computation. The time-optimal universal control of two-qubit system has been realized in diamond with high fidelity.

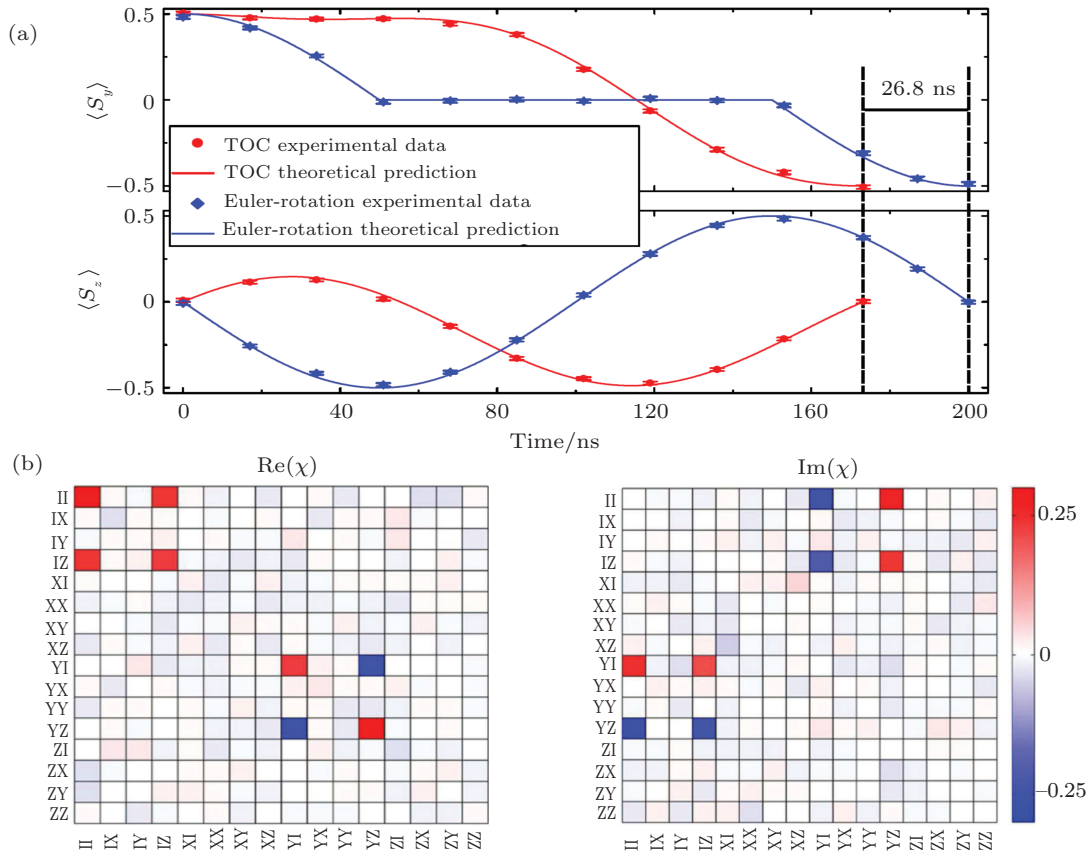


Fig. 12. (a) State evolutions during $R(\hat{\boldsymbol{z}}, \pi)$ with TOC and Euler rotation. The initial state is $(|m_s = 0\rangle + \mathrm{i}|m_s = -1\rangle)/\sqrt{2}$. The gate time of TOC is 26.8 ns shorter than that of Euler rotation. (b) Quantum process tomography for the controlled-U gate by TOC. The left and right panels are the real and imaginary parts of the reconstructed process matrix χ. The error bar of each point is about 0.01 due to the statistics of photon counts. An average gate fidelity of 0.99(1) can be obtained from the process matrix. Adapted from Ref. [96]. ©2016 by the American Physical Society.

3.4. Adiabatic quantum factorization algorithm

After reviewing the quantum coherent optimal control technique, we discuss another different quantum computation, *i.e.*, the adiabatic quantum computing (AQC). It has been proposed by Farhi *et al.*[98] in 2000. The basic idea of this architecture is that the computational process can be realized by the adiabatic evolution of a system's Hamiltonian and regarded as circuit model quantum computing.[99] As a universal and robust method of quantum computing, the AQC can solve the problem by adiabatically evolving the quantum processor from the ground state of a simple initial Hamiltonian to that of a final one, which encodes the solution of the problem. In quantum computing, a quantum algorithm is an algorithm that runs on a realistic model of quantum computing. One of the reason we are interested in quantum algorithms is that it can solve some problems faster than classical algorithms. For multiplying of large prime numbers, up to now, no efficient classical algorithm can factorize this large numbers.[100] A lot of experimental work on large number factorization has been done either based on Shor's algorithm[101–107] or based on the AQC architecture with ensemble systems.[108,109] Adiabatic quantum factorization algorithm was developed by Burges *et al.*[110] for the first time. An improved version was realized by Xu *et al.*[108] Based on this version, the factorization of 35 on the adiabatic quantum processor with single spin has been reported at room temperature.[111] The main idea used here is to transform a factorization problem into an optimization problem and solve it under the AQC framework.

In the AQC framework, we first need to find a problem Hamiltonian $H_{\rm p}$ to solve a problem and the solution of the problem is encoded in the ground state of $H_{\rm p}$. Let us get started from the ground state of H_0, the Hamiltonian of the evolution progress can be written as

$$\begin{aligned} &H(t) = (1-s(t))H_0 + s(t)H_{\rm p}, \\ &s(0) = 0,\ s(T) = 1. \end{aligned} \tag{22}$$

where T is the total evolution time, and the whole system is evolved under the Schrödinger equation

$$\mathrm{i}\frac{\mathrm{d}}{\mathrm{d}t}|\psi(t)\rangle = H(t)|\psi(t)\rangle. \tag{23}$$

Based on the adiabatic theorem, if the system evolves slowly enough, *i.e.*, $T \gg 1/g_{\min}^2$, where $g_{\min}^2$ is the minimum spectral gap of $H(t)$, it tends to stay on the ground state of $H(t)$. When it is close to $t = T$, the system is on the ground state of $H(T)$ and gives the solution of the problem. According to the multiplication table (see Table 1), an equation set can be constructed. To solve these equations with fewer qubits, it can be simplified by using some logical constraints.

Table 1. Multiplication table for $5 \times 7 = 35$ in binary. The top row represents the significance of each bit. x and y are the multipliers. z_{ij} is the carry bit from the i-th bit to the j-th bit, and the row in the bottom is the number we want to factor, *i.e.*, 35. This table is adapted from Ref. [111]. ©2017 by the American Physical Society.

	2^5	2^4	2^3	2^2	2^1	2^0
x				1	p	1
y				1	q	1
				1	p	1
			q	pq	q	
		1	p	1		
Carries	z_{45}	z_{34}	z_{23}	z_{12}		
	z_{35}	z_{24}				
$x \times y = 35$	1	0	0	0	1	1

After the simplification (see Ref. [111] for more details), the result can be written as

$$p + q = 1, \tag{24}$$

and the simplification do not increase the complexity of the quantum algorithm. Based on the idea of Burges *et al.*,[110] the problem Hamiltonian is

$$H_{\rm p} = \left(\frac{I-\sigma_{1,z}}{2} + \frac{I-\sigma_{2,z}}{2} - I\right)^2 = (S_z + I_z)^2, \tag{25}$$

where $\sigma_{1,z}$ and $\sigma_{2,z}$ are replaced with S_z and I_z, *i.e.*, the electron and nuclear spin operators, respectively. Then one can drop the identity operator and scale it with a constant g_1

$$H_{\rm p} = g_1(2S_zI_z). \tag{26}$$

The H_0 should be noncommutative with $H_{\rm p}$, otherwise there will be energy level crossings. Generally, H_0 can be written as

$$H_0 = g_2(S_x + I_x). \tag{27}$$

The experiment was carried out in Type-IIa bulk diamond samples with nitrogen impurity concentration < 5 ppb and ^{13}C isotope of natural abundance (1.1%). With the direction of the external magnetic field aligned along the symmetry axis, the Hamiltonian of the NV center electron spin coupled with the ^{14}N nuclear spin is

$$H = D{S_z}^2 + \gamma_e B_z S_z + Q{I_z}^2 + \gamma_n B_z I_z + \hat{S}\tilde{A}\hat{I}, \tag{28}$$

where $Q = -4.95$ MHz is the nuclear quadrupolar splitting and $\tilde{A}$ is the hyperfine interaction tensor between the electron spin and the nuclear spin. Here, one picked 4 out of 9 levels to perform the experiment and encoded them as two qubits.

In order to overcome the limitation of coherent time, the optimal control is used to replace the adiabatic evolution part, which is robust to noise and guarantees high fidelity. The adiabaticity of the whole process is reflected in the evolution with six measurements of the diagonal elements, as exhibited

in Fig. 13. The lines and dots show the results of theoretical calculations and experimental measurements, respectively. The deviation here comes from the imperfect initialization and control pulses. The population of the final state concentrates on $|01\rangle$ and $|10\rangle$, which indicates that the solution of the factorization problem is $\{p=0,\ q=1\}$ or $\{p=1,\ q=0\}$, *i.e.*, the multipliers are $\{x=5,\ y=7\}$ or $\{x=7,\ y=5\}$. The fidelity between the experimental and the ideal final state $\Psi_{\rm f}=\frac{1}{\sqrt{2}}(|01\rangle+|10\rangle)$ is 0.81(6). It is worth mentioning that to achieve the optimal control of the hybrid spin system, not only did we use a shaping pulse, but also both the shaping pulses of electrons and nuclear spins were applied for the first time.[111] For experimentally factored 35 and the results with high fidelity, the optimal control technology has been used and it is also used on an electron–nuclear hybrid system, which is considered to be challenging due to the large mismatch of the electron and nuclear spin gyromagnetic ratio.[111] The arbitrary factorization of large numbers is related to the scalability of the method, which is very promising, but there are still several challenges.[111] The optimal control technique can also be extended to other single-spin systems because they[112–114] share a similar control method based on spin magnetic resonance.

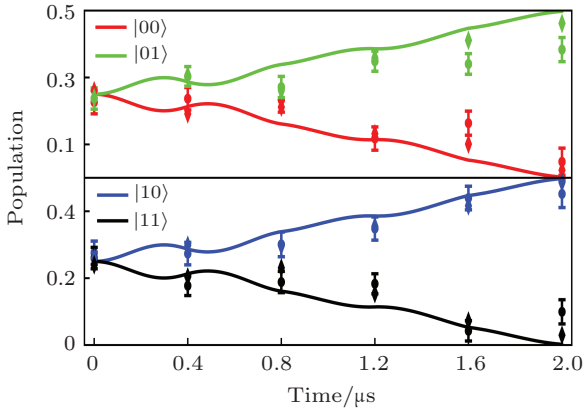


Fig. 13. The populations on computational basis of the system during the process of the adiabatic factorization. The lines are theoretical predictions with prefect initialization and control. The diamonds are the theoretical calculations taking imperfect initialization and control into consideration, and the dots are obtained from experimental data. Adapted from Ref. [111]. ©2017 by the American Physical Society.

4. On experimental implementations and tests of the uncertainty principle

Based on the previous work, we study some fundamental problem such as Heisenberg's uncertainty relation in spin system. The principle of uncertainty was first proposed by Heisenberg in his thought experiment, indicating that the measurement of the electron's position inevitably interfered with the momentum.[115] In the following years, Kennard,[116] Robertson,[117] and Schrödinger [118] mathematically derived tight relations, such as the famous Heisenberg–Robertson uncertainty relation [117]

$$\Delta A\Delta B \geq \frac{1}{2}|\langle[A,B]\rangle|, \tag{29}$$

with the standard deviation $\Delta\Omega=\sqrt{\langle\Omega^2\rangle-\langle\Omega\rangle^2}$ for the observable $\Omega=A$ or B, the angle brackets $\langle\ \rangle$ denoting the expectation of an operator with respect to a given state ρ, and $[A,B]=AB-BA$. The inequality imposes a trade-off between the statistical dispersions ΔA and ΔB of the pair of non-commuting observables A and B for the given quantum state ρ. The most commonly cited version of uncertainty relation is preparation uncertainty relation, dealing with the spread of measurement outcomes rather than Heisenberg's original idea which investigates measurement inaccuracies.[119–126] There is a long history of trying to quantify Heisenberg's original ideas.[119] More than a decade ago, a universally valid error–disturbance relation was proved by Ozawa.[127] Not long after, Hall and Ozawa showed that any joint measurements would estimate the inaccuracy of two incompatible observables to satisfy similar relations.[128–130] Later, Branciard[130,131] and Weston *et al.*[133] derived the tighter inequalities. These relations have been experimentally verified with polarized neutrons[134,135] and photons.[133,136–139] However, the physical validity of the definitions of error and disturbance in Ozawa's relation is controversial.[120,121,140–144] Buscemi *et al.*[123] introduced information-theoretic definitions for noise and disturbance and derived a state-independent tradeoff relation. This relation has been verified by neutron spin qubits.[124] Although uncertainty principle can be described with different relations,[145,146] uncertainty relations between two observables are still well known. There are long history attempts to encompass three or more observables since Robertson's work in 1934.[147–150] Compared with two-observable relation in Eq. (29) which can be derived via the Cauchy–Schwarz inequality, it is difficult to obtain a nontrivial multi-observable uncertainty relation similar to Eq. (29). We will briefly comment on these two aspects of uncertainty relations below.

4.1. Uncertainty relation based on statistical distances

Recently, uncertainty relations dealing with the imprecisions in joint measurements approximating incompatible observables have been formulated by Busch, Lahti, and Werner (BLW).[120–122] Their results also apply to successive measurements, which are encompassed by joint measurement scenarios. The imprecisions or uncertainties, based on statistical distances between probability distributions of measurement outcomes are processed into state-independent and regarded as figures of merit of joint-measurement devices. According to BLW's theoretical framework, an improved relation for qubit

measurement and experimental test has been reported[125] in a spin system using the NMR technique.

A and B are a pair of incompatible observables we consider. Incompatible means A and B cannot be jointly measured, *i.e.*, can not be measured simultaneously. For qubit measurements, A and B can be chosen as the two sharp observables with the spectral projections $A_\pm = (\mathbb{1} \pm \boldsymbol{a}\cdot\boldsymbol{\sigma})/2$ and $B_\pm = (\mathbb{1} \pm \boldsymbol{b}\cdot\boldsymbol{\sigma})/2$, where $\boldsymbol{a}$ and $\boldsymbol{b}$ are unit vectors. If $\boldsymbol{a}$ and $\boldsymbol{b}$ are non-collinear, the observables A and B are incompatible. A device composed of compatible observables C and D (each being used as an approximation of A and B) can be used to approximately measure A and B simultaneously. The observable C consists of positive operators $C_+ = (c_0\mathbb{1} + \boldsymbol{c}\cdot\boldsymbol{\sigma})/2$, $C_- = \mathbb{1} - C_+$, with $|\boldsymbol{c}| \le \min\{c_0, 2-c_0\} \le 1$ for the positivity. Similarly, the observable D consists of $D_+ = (d_0\mathbb{1} + \boldsymbol{d}\cdot\boldsymbol{\sigma})/2$, $D_- = \mathbb{1} - D_+$, with $|\boldsymbol{d}| \le \min\{d_0, 2-d_0\} \le 1$. Compatible or jointly measurable requires that there exists a positive-operator valued measure (POVM) M of which C and D are the marginals, namely, $C_i = \sum_j M_{ij}$ and $D_j = \sum_i M_{ij}$, with $i, j = +$ or $-$ (hereinafter the same) and $M_{ij} = (C_i D_j + D_j C_i)/2$. When $c_0 = d_0 = 1$, the criterion of compatibility has been simplified as[121,151,152]

$$|\boldsymbol{c} + \boldsymbol{d}| + |\boldsymbol{c} - \boldsymbol{d}| \le 2. \tag{30}$$

Compatibility permits C and D to be measured simultaneously, but imposes a strong limitation against C and D approaching A and B freely. The overall deviation of C and D from A and B, or the performance of the device, is rooted in probability distributions of measurement outcomes.

The operators $O_\pm$ ($O = A$, B, C, and D) are called effects and the probabilities of measurement outcomes are $p^O_\pm = \mathrm{Tr}(\rho O_\pm)$, where $\rho = (\mathbb{1} + \boldsymbol{r}\cdot\boldsymbol{\sigma})/2$ is the density operator of a qubit. Take outcomes of these measurements to be ± 1, then the observable O is given as a map $\pm 1 \mapsto O_\pm$. The statistical difference between the measurements of A and C, in other words the inaccuracy or uncertainty, can be quantified as $\delta_\rho(A,C) := 2\sum_i \left|p^A_i - p^C_i\right| = 2\left|1 - c_0 + \boldsymbol{r}\cdot(\boldsymbol{a} - \boldsymbol{c})\right|$.[121] In a similar way, the statistical difference between the measurements of B and D can be expressed as $\delta_\rho(B,D) := 2\sum_i \left|p^B_i - p^D_i\right| = 2\left|1 - d_0 + \boldsymbol{r}\cdot(\boldsymbol{b} - \boldsymbol{d})\right|$. Since the observables C and D are jointly measured, they face the same quantum state ρ and the combined difference $\Delta_\rho(A,B;C,D) := \delta_\rho(A,C) + \delta_\rho(B,D)$ is the inaccuracy of the joint measurement for a specific state. The state-dependent quantity $\Delta_\rho(A,B;C,D)$ has a vanishing lower bound for any given A, B, and ρ. In other words, $\Delta_\rho(A,B;C,D)$ becomes zero when minimizing over all C and D for any given A, B, and ρ (see Section II.A in Ref. [125]). By maximizing $\Delta_\rho(A,B;C,D)$ over all ρ, one obtains $\Delta(A,B;C,D) := \max_\rho \Delta_\rho(A,B;C,D)$ as the worst-case inaccuracy of the joint measurement. The state-independent quantity $\Delta(A,B;C,D)$ characterizes the integrated deviation of C and D from A and B and thus is a figure of merit of the measurement device. The inaccuracy trade-off relation can be written as

$$\begin{aligned}\Delta(A,B;C,D) &:= \max_\rho \left[\delta_\rho(A,C) + \delta_\rho(B,D)\right] \\ &\ge \Delta_{\mathrm{lb}}(A,B) := |\boldsymbol{a} + \boldsymbol{b}| + |\boldsymbol{a} - \boldsymbol{b}| - 2,\end{aligned} \tag{31}$$

as shown in Fig. 14(a). The lower bound $\Delta_{\mathrm{lb}}(A,B)$ is the amount of violation of the inequality in Eq. (30), and is termed as the degree of incompatibility of A and B.[121] This lower bound is attained when C and D are the best approximations of A and B, and such C and D have $c_0 = d_0 = 1$ and $\boldsymbol{c}, \boldsymbol{d}$ depicted in Fig. 14(c).

Compared with BLW's original relation, the characteristic quantity $\Delta(A,B;C,D)$ possesses an explicit physical meaning as the worst-case inaccuracy and has a delicate lower bound without an additional coefficient (see Section II.B in Ref. [125]). Besides, as a modification of BLW's basic framework, the improved approach also applies to any pair of incompatible observables like position and momentum, although the combined inaccuracy might not be in the additive form. Experimental demonstration of the relation in Eq. (31) has been implemented in the nuclear spin system,[125] operating on a 400 MHz liquid-state nuclear magnetic resonance spectrometer. In the experiment, the diethyl fluoromalonate was used as the sample dissolved in ^{2}H-labeled chloroform at 304 K. The ^{19}F, ^{1}H, and ^{13}C nuclear spins serve as the system, ancilla, and probe qubits, respectively. The device is simulated by joint measurement that measures two compatible observables at the same time. Several configurations of A,B and C,D with all the Bloch vectors in the xz plane have been chosen. Every pair of $\boldsymbol{a}$ and $\boldsymbol{b}$ is symmetric about the z axis, and is expressed as $\boldsymbol{a} = (-\sin(\theta/2), \cos(\theta/2))$, $\boldsymbol{b} = (\sin(\theta/2), \cos(\theta/2))$, where the former and latter components of a vector correspond to x and z, respectively (hereinafter the same). In the case where $\theta = 90^\circ$, the vectors $\boldsymbol{a}$ and $\boldsymbol{b}$ are perpendicular to each other and the relevant observables A and B are maximally incompatible. Consider a series of compatible observables C and D with $\boldsymbol{c} = \left(-\sin\gamma\cos\gamma, \sin^2\gamma\right)$, $\boldsymbol{d} = \left(\sin\gamma\cos\gamma, \cos^2\gamma\right)$ as illustrated in Fig. 15(a). The inaccuracy Δ varies with γ and is bounded by $\Delta_{\mathrm{lb}} = 2\left(\sqrt{2} - 1\right) \approx 0.83$ as shown in Fig. 15(b). When $\gamma = 45^\circ$, the corresponding C and D are the optimal approximations to A and B, and the inaccuracy Δ reaches its lower bound Δ_{lb}. The statistics of measurement outcomes for two instances where $\gamma = 15^\circ$ and 45° are listed in Figs. 15(c) and 15(d) which visually support the superiority of the optimal C and D. All the experimental results confirm the inaccuracy trade-off relation in Eq. (31).

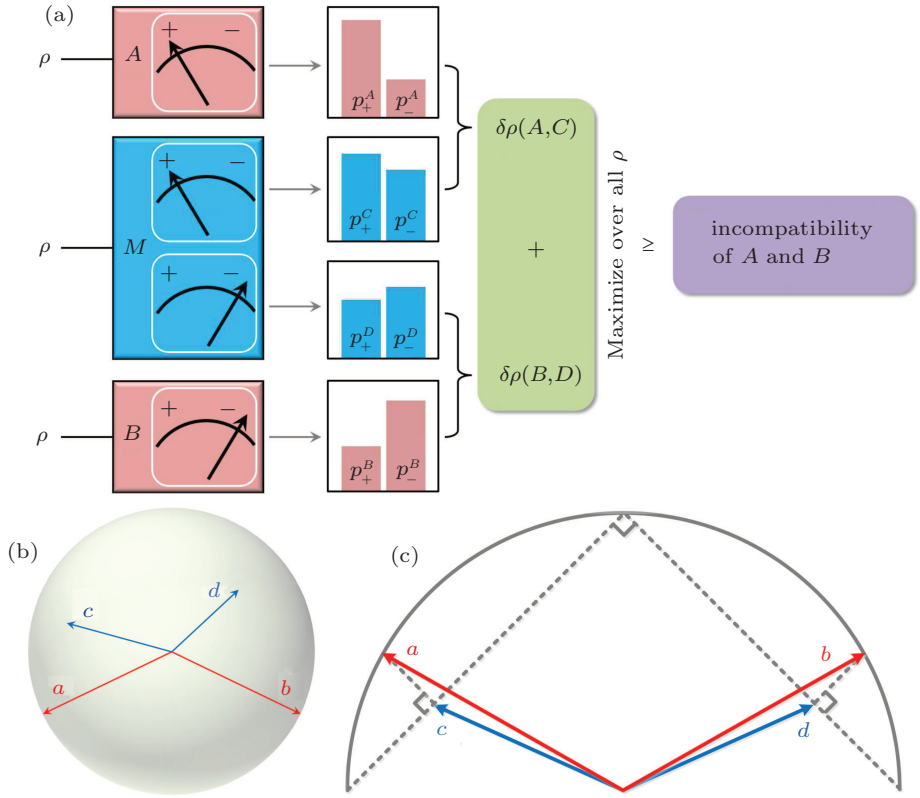


Fig. 14. Sketch of the theory. (a) Outline of the inaccuracy trade-off relation in Eq. (31). Here, compatible observables C and D are jointly measured to approximate incompatible observables A and B. (b) An example of Bloch vectors $\boldsymbol{a}, \boldsymbol{b}, \boldsymbol{c}$, and $\boldsymbol{d}$. The lengths of $\boldsymbol{c}$ and $\boldsymbol{d}$ are usually less than 1. (c) Bloch vectors $\boldsymbol{c}$ and $\boldsymbol{d}$ of the optimal compatible observables C and D that approximate A and B. The dashed lines are legs of an inscribed isosceles right triangle. The vectors $\boldsymbol{a}-\boldsymbol{c}$ and $\boldsymbol{b}-\boldsymbol{d}$ are orthogonal to these dashed lines, and the end points of $\boldsymbol{c}$ and $\boldsymbol{d}$ are the perpendicular feet. The whole pattern is coplanar and symmetric. Adapted from Ref. [125]. ©2016 by the American Physical Society.

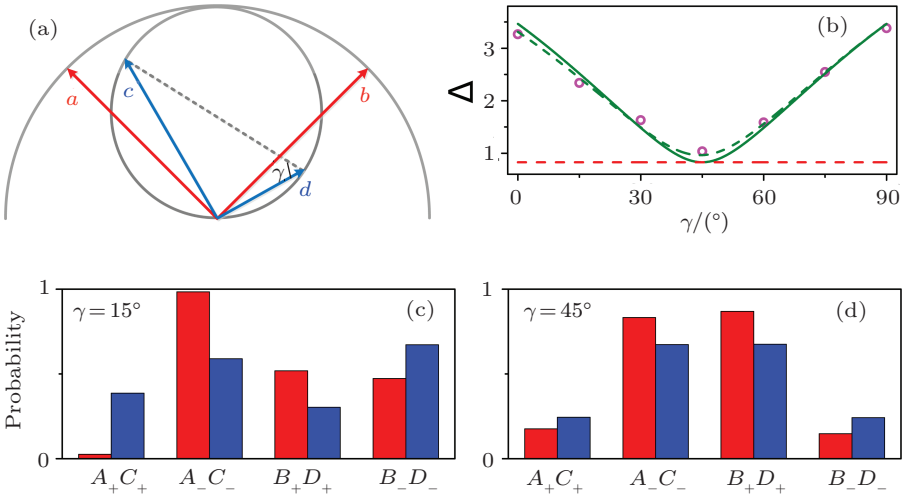


Fig. 15. Experimental demonstration of the inaccuracy trade-off relation with maximally incompatible A and B. (a) Bloch vectors of observables. The whole configuration is coplanar. The vectors $\boldsymbol{a}$ and $\boldsymbol{b}$ are mutually perpendicular and incline symmetrically about the vertical direction, which is the z direction. The end points of vectors $\boldsymbol{c}$ and $\boldsymbol{d}$ are the diameter ends of the small circle which is internally tangent to the semicircle and passes through its center. The center of the semicircle is the origin and the tangent point is in the z axis. (b) The inaccuracy Δ as a function of the angle $\gamma = \arctan(|\boldsymbol{c}|/|\boldsymbol{d}|)$. The circles, solid curves, and dashed curves represent the measured, theoretical, and simulated values of Δ, respectively. The numerical simulation takes decoherence into account. The dashed straight line denotes the lower bound Δ_{lb}. (c) and (d) The statistics of measurement outcomes for $\gamma = 15°$ and $45°$. Adapted from Ref. [125]. ©2016 by the American Physical Society.

4.2. Uncertainty relations for the triple components of angular momentum

Recently, an uncertainty relation for three pairwise canonical observables p, q, and r satisfying $[p,q] = [q,r] = [r,p] = -\mathrm{i}\hbar$ with $r = -p - q$ was derived by Kechrimparis and Weigert.[153] Here, p and q are the momentum and position, respectively. From the inequality in Eq. (29), one immediately obtains $\Delta p \Delta q \geq \hbar/2$, $\Delta q \Delta r \geq \hbar/2$, and $\Delta r \Delta p \geq \hbar/2$. By multiplying these inequalities and taking the square root, one gets $\Delta p \Delta q \Delta r \geq (\hbar/2)^{3/2}$. However, this inequality is not tight. In

other words, there is no state satisfying such lower bound. By introducing the triple constant $\tau = 2/\sqrt{3}$, the tight triple uncertainty relation $\Delta p\Delta q\Delta r \geq (\tau\hbar/2)^{3/2}$ is established. Compared with two observables p and q, the latecomer r looks artificial and should not exhibit a particular physical meaning. Yet the three components of angular momentum form a natural triple.[154]

The lower bound for spin-1/2 has been tightened by introducing the triple constant τ[34], *i.e.*,

$$\Delta S_x \Delta S_y \Delta S_z \geq \left| \frac{\tau^3}{8} \langle S_x \rangle \langle S_y \rangle \langle S_z \rangle \right|^{1/2}, \tag{32}$$

where S_x, S_y, and S_z are the angular momentum operators and satisfying commutation relations $[S_x, S_y] = \mathrm{i}S_z$, $[S_z, S_x] = \mathrm{i}S_y$, and $[S_y, S_z] = \mathrm{i}S_x$. The equality in Eq. (32) holds when $|r_x| = |r_y| = |r_z| = 1/\sqrt{3}$ or $(|r_x| - 1)(|r_y| - 1)(|r_z| - 1) = 0$. Here, r_x, r_y, and r_z are the components of the Bloch vector $\boldsymbol{r}$ of a qubit state with the density matrix $\rho = (\mathbb{1} + \boldsymbol{r} \cdot \boldsymbol{\sigma})/2$. The lower bound is also tightened by introducing the triple constant τ, *i.e.*,

$$(\Delta S_x)^2 + (\Delta S_y)^2 + (\Delta S_z)^2 \geq \frac{\tau}{2} \left(|\langle S_x \rangle| + |\langle S_y \rangle| + |\langle S_z \rangle| \right). \tag{33}$$

The equality in Eq. (33) is attained if and only if $|r_x| = |r_y| = |r_z| = 1/\sqrt{3}$ for spin-1/2. The uncertainty relations in Eqs. (32) and (33) have state-dependent lower bounds. It is similar for uncertainty relations with state-independent lower bounds. The pairwise inequalities for spin-1/2,[121] namely, $(\Delta S_x)^2 + (\Delta S_y)^2 \geq 1/4$, $(\Delta S_y)^2 + (\Delta S_z)^2 \geq 1/4$, and $(\Delta S_z)^2 + (\Delta S_x)^2 \geq 1/4$, immediately yield the inequality $(\Delta S_x)^2 + (\Delta S_y)^2 + (\Delta S_z)^2 \geq 3/8$ which is not tight. A tight lower bound needs an additional factor τ^2[148,155] written as

$$(\Delta S_x)^2 + (\Delta S_y)^2 + (\Delta S_z)^2 \geq \frac{1}{2} = \frac{3}{8}\tau^2. \tag{34}$$

The equality is established only $|\boldsymbol{r}| = 1$, in other words, the qubit is in a pure state.

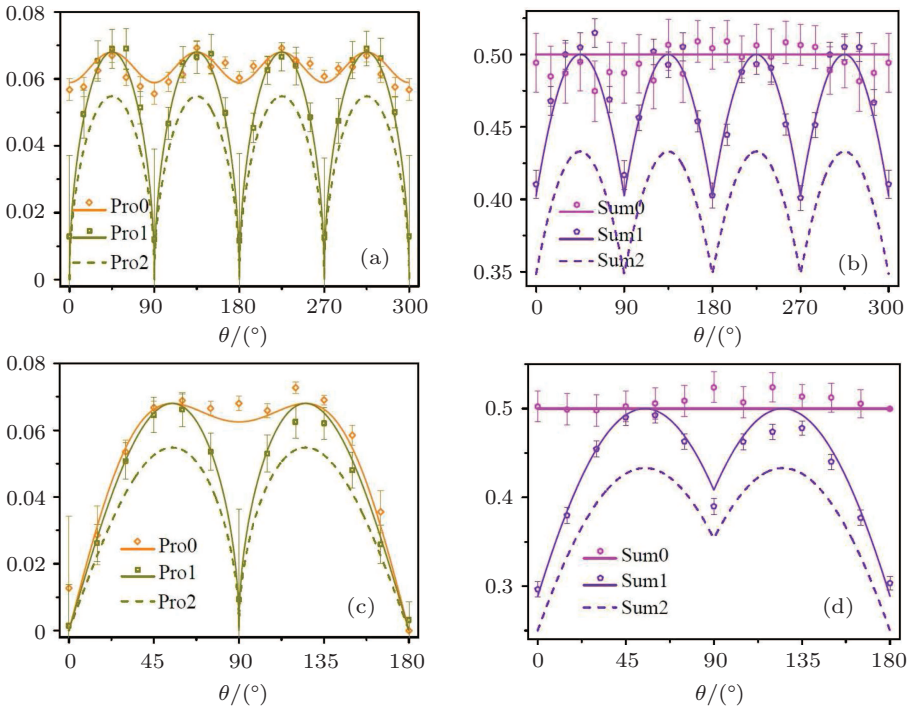


Fig. 16. Experimental results. (a) Experimental demonstration for the uncertainty relation of the multiplicative form. The solid orange, solid green, and dashed green curves, in turn, represent the theoretical values of Pro0, Pro1, and Pro2, where Pro0 $= \Delta S_x \Delta S_y \Delta S_z$, Pro1 $= \left|\tau^3 \langle S_x \rangle \langle S_y \rangle \langle S_z \rangle / 8\right|^{1/2}$, and Pro2 $= \left|\langle S_x \rangle \langle S_y \rangle \langle S_z \rangle / 8\right|^{1/2}$. The orange and green scattered points represent the experimental value of Pro0 and Pro1, respectively. (b) Experimental demonstration for the uncertainty relations of the additive form. The solid magenta, solid violet, and dashed violet curves, in turn, represent the theoretical values of Sum0, Sum1, and Sum2, where Sum0 $= (\Delta S_x)^2 + (\Delta S_y)^2 + (\Delta S_z)^2$, Sum1 $= \tau\left(|\langle S_x \rangle| + |\langle S_y \rangle| + |\langle S_z \rangle|\right)/2$, and Sum2 $= \left(|\langle S_x \rangle| + |\langle S_y \rangle| + |\langle S_z \rangle|\right)/2$. The magenta and violet scattered points represent the experimental value of Sum0 and Sum1, respectively. Error bars represent ± 1 s.d. (c) Experimental demonstration for the uncertainty relation of the multiplicative form. (d) Experimental demonstration for the uncertainty relations of the additive form. Adapted from Ref. [34]. ©2017 by the American Physical Society.

Experimental verification of uncertainty relations in Eqs. (32) and (33) was reported[34] in an NV center in diamond (use a bulk sample with the ^{13}C nuclide at the natural abundance of about 1.1% and the nitrogen impurity less than 5 ppb). In this experiment, two series of pure states $|\psi\rangle$ with Bloch vectors $\boldsymbol{r}_1 = \left(\sqrt{2/3}\cos\varphi, \sqrt{2/3}\sin\varphi, 1/\sqrt{3}\right)$ and $\boldsymbol{r}_2 = \left(\sin\theta/\sqrt{2}, \sin\theta/\sqrt{2}, \cos\theta\right)$ were chosen; see Ref. [34] for more details about the expectations of S_x, S_y, and S_z. The verification of the multiplicative uncertainty relation in Eq. (32) is shown in Figs. 16(a) and 16(c). The results

demonstrate that for the product $\Delta S_x \Delta S_y \Delta S_z$, the lower bound with the triple constant τ, namely, $\left|\tau^3 \langle S_x\rangle\langle S_y\rangle\langle S_z\rangle/8\right|^{1/2}$, outperforms the naive lower bound without the triple constant, namely, $\left|\langle S_x\rangle\langle S_y\rangle\langle S_z\rangle/8\right|^{1/2}$. The results for the sum $(\Delta S_x)^2 + (\Delta S_y)^2 + (\Delta S_z)^2$ are shown in Figs. 16(b) and 16(d). The lower bound with the triple constant τ, namely, $\tau\left(|\langle S_x\rangle| + |\langle S_y\rangle| + |\langle S_z\rangle|\right)/2$, outperforms the naive one without the triple constant, namely, $\left(|\langle S_x\rangle| + |\langle S_y\rangle| + |\langle S_z\rangle|\right)/2$. The same results also support the derivation[148,155] of the uncertainty relation in Eq. (34). Therefore, the triple uncertainty relations in Eqs. (32), (33), and (34) are confirmed by the experimental results. This work can consistently support the theoretical results and enrich the uncertainty relations of more than two observables.

5. Brief conclusions

Quantum coherence plays an important role in quantum information theory, quantum thermodynamics, and quantum biology, as well as physics more widely; therefore, it is interesting to study the coherence and its protection in various systems such as spin systems. In order to perform long coherence time quantum computations, a thorough understanding and suppression of decoherence are badly needed, together with quantum error correction and fault-tolerant quantum computation schemes. Isolated electron spin in the diamond nitrogen-vacancy center has proven to be a unique and promising candidate for solid-state quantum computing.

In summary, this work presents a concise review on the field of quantum coherence and uncertainty relation in spin systems. The coherence can be preserved by several strategies such as reducing the nuclear spins in the environment, cooling the temperatures, and performing dynamical decoupling operations. In addition, the coherence can be applied to the weak magnetic fields detection with high spatial resolution. In recent years, research on various type uncertainty relations has been expanding with an increasing rate. In spite of the basic principle in quantum mechanics, uncertainty relation has demonstrated to be a fruitful concept both for fundamental studies and for designing novel experimental techniques. Potential applications of quantum coherence include such diverse topics as quantum computation, quantum communication, and quantum information processing. The experimental research of coherent spin developed here will provide insights and a useful guide for further applications of coherence.

References

[1] Wang Y, Liu R B and Sham L J 2006 *Phy. Rev. B* **74** 195301
[2] Hahn E L 1950 *Phys. Rev.* **80** 580
[3] Schweiger H and Jeschke G 2001 *Principles of Pulse Electron Paramagnetic Resonance* (Oxford: Oxford University Press)
[4] Morton J J L, Tyryshkin A M, Ardavan A, Benjamin S C, Porfyrakis K, Lyon S A and Briggs G A D 2006 *Nat. Phys.* **2** 40
[5] Khodjasteh K and Lidar D A 2006 *Phys. Rev. Lett.* **95** 180501
[6] Santos L F and Viola L 2006 *Phys. Rev. Lett.* **97** 150501
[7] Yao W, Liu R B and Sham L J 2006 *Phys. Rev. Lett.* **98** 077602
[8] Witzel W M and Sarma S D 2007 *Phys. Rev. B* **76** 241303
[9] Uhrig G S 2007 *Phys. Rev. Lett.* **98** 100504
[10] Yang W and Liu R B 2008 *Phys. Rev. Lett.* **101** 180403
[11] Viola L, Knill E and Lloyd S 1999 *Phys. Rev. Lett.* **82** 2417
[12] Du J F, Rong X, Zhao N, Wang Y, Yang J H and Liu R B 2009 *Nature* **461** 265
[13] Wang Y, Rong X, Feng P B, Xu W J, Chong B, Su J H, Gong J B and Du J F 2011 *Phys. Rev. Lett.* **106** 040501
[14] Wootters W K 1998 *Phys. Rev. Lett.* **80** 2245
[15] Chiba M and Hirai A 1972 *J. Phys. Soc. Jpn.* **33** 730
[16] Tyryshkin A M, Lyon S A, Astashkin A V and Raitsimring A M 2003 *Phys. Rev. B* **68** 193207
[17] Rong X, Wang Z X, Jin F Z, Geng J P, Feng P B, Xu N Y, Wang Y, Ju C Y, Shi M J and Du J F 2012 *Phys. Rev. B* **86** 104425
[18] Rong X, Jin F Z, Wang Z X, Geng J P, Ju C Y, Wang Y, Zhang R M, Duan C K, Shi M J and Du J F 2013 *Phys. Rev. B* **88** 054419
[19] Anderson P W 1954 *J. Phys. Soc. Jpn.* **9** 316
[20] Kubo R 1954 *J. Phys. Soc. Jpn.* **9** 935
[21] Berman P R and Brewer R G 1985 *Phys. Rev. A* **32** 2784
[22] Loring R F and Mukamel S 1985 *Chem. Phys. Lett.* **114** 426
[23] Zhao N, Wang Z Y and Liu R B 1998 *Phys. Rev. Lett.* **106** 217205
[24] Huang P, Kong X, Zhao N, Shi F Z, Wang P F, Rong X, Liu R B and Du J F 2011 *Nat. Commun.* **2** 570
[25] Maze J R, Taylor J M and Lukin M D 2008 *Phys. Rev. B* **78** 094303
[26] Zhao N, Hu J L, Ho S W, Wan J T K and Liu R B 2011 *Nat. Nanotech.* **6** 242
[27] Zhao N, Ho S W and Liu R B 2012 *Phys. Rev. B* **85** 115303
[28] Lange G D, Wang Z, Riste D, Dobrovitski V V and Hanson R 2010 *Science* **330** 60
[29] Ryan C A, Hodges J S and Cory D G 2010 *Phys. Rev. Lett.* **105** 200402
[30] Naydenov B, Dolde F, Hall L T, Shin C, Fedder H, Hollenberg L C, Jelezko F and Wrachtrup J 2011 *Phys. Rev. B* **83** 081201
[31] Taylor J M, Cappellaro P, Childress L, Jiang L, Budker D, Hemmer P R, Yacoby R A, Walsworth R and Lukin M D 2008 *Nat. Phys.* **4** 810
[32] Loubser J H N and Wyk J A V 1977 *Diamond Research* **11** 4
[33] Loubser J H N and Wyk J A V 1978 *Rep. Prog. Phys.* **41** 1201
[34] Ma W C, Chen B, Liu Y, Wang M Q, Ye X Y, Kong F, Shi F Z, Fei S M and Du J F 2017 *Phys. Rev. Lett.* **118** 180402
[35] Robledo L, Childress L, Bernien H, Hensen B, Alkemade P F A and Hanson R 2011 *Nature* **477** 574
[36] Maze J R, Stanwix P L, Hodges J S, Hong S, Taylor J M, Cappellaro P, Jiang L, Dutt M V G, Togan E, Zibrov A S, Yacoby A, Walsworth R L and Lukin M D 2008 *Nature* **455** 644
[37] Balasubramanian G, Neumann P, Twitchen D, Markham M, Kolesov R, Mizuochi N, Beck J, Tissler J, Jacques V, Hemmer P R, Jelezko F and Wrachtrup J 2009 *Nat. Mater.* **8** 383
[38] Zhao N, Honert J, Schmid B, Klas M, Isoya J, Markham M, Twitchen D, Jelezko F, Liu R B, Fedder H and Wrachtrup J 2012 *Nat. Nanotech.* **7** 657
[39] Taminiau H T, Wagenaar J J T, Sar T V D, Jelezko F, Dobrovitski V V and Hanson R 2012 *Phys. Rev. Lett.* **109** 137602
[40] Kolkowitz S, Unterreithmeier Q P, Bennett S D and Lukin M D 1998 *Phys. Rev. Lett.* **109** 137601
[41] Ma W C, Shi F Z, Xu K B, Wang P F, Xu, X K, Rong X, Ju C Y, Duan C K, Zhao N and Du J F 2015 *Phys. Rev. A* **92** 033418
[42] London P, Scheuer J, Cai J M, Schwarz I, Retzker A, Plenio M B, Katagiri M, Teraji T, Koizumi S, Isoya J, Fischer R, McGuinness L P, Naydenov B and Jelezko F 2013 *Phys. Rev. Lett.* **111** 067601
[43] Perunicic V S, Hall L T, Simpson D A, Hill C D and Hollenberg L C L 1998 *Phys. Rev. B* **89** 054432
[44] Cai J M, Jelezko F, Plenio M B and Retzker A 2013 *New J. Phys.* **15** 013020
[45] Ofori-Okai K B, Pezzagna S, Chang K, Loretz M, Schirhagl R, Tao Y, Moores B A, Groot-Berning K, Meijer J and Degen C L. 2012 *Phys. Rev. B* **86** 081406

[46] Ohashi K, Rosskopf T, Watanabe H, Loretz M, Tao Y, Hauert R, Tomizawa S, Ishikawa T, Ishi-Hayase J, Shikata S, Degen C L and Itoh K M 2013 *Nano Lett.* **13** 4733

[47] Staudacher T, Shi F, Pezzagna S, Meijer J, Du J, Meriles C A, Reinhard F and Wrachtrup J 2013 *Science* **339** 561

[48] Mamin J H, Kim M, Sherwood M H, Rettner C T, Ohno K, Awschalom D D and Rugar D 2013 *Science* **339** 557

[49] Müller C, Kong X, Cai J M, Melentijević K, Stacey A, Markham M, Twitchen D, Isoya J, Pezzagna S, Meijer J, Du J F, Plenio M B, Naydenov B, McGuinness L P and Jelezko F 2014 *Nat. Commun.* **5** 4703

[50] Sushkov A O, Lovchinsky I, Chisholm N, Walsworth R L, Park H K and Lukin M D 2014 *Phys. Rev. Lett.* **113** 197601

[51] Lovchinsky I, Sushkov A O, Urbach E, Leon N P D, Choi S, Greve K D, Evans R, Gertner R, Bersin E, Müller C, McGuinness L, Jelezko F, Walsworth R L, Park H and Lukin M D 2016 *Science* **351** 836

[52] Shi F Z, Kong X, Wang P F, Kong F, Zhao N, Liu R B and Du J F 2014 *Nat. Phys.* **10** 21

[53] Borbat P P, Costa-Filho A J, Earle K A, Moscicki J K and Freed J H 2001 *Science* **291** 266

[54] Rugar D, Budakian R, Mamin H J and Chui B W 2004 *Nature* **430** 329

[55] Xiao M, Martin I, Yablonovitch E and Jiang H W 2004 *Nature* **430** 435

[56] Manassen Y, Hamers R, Demuth J and Castellano A 1989 *Phys. Rev. Lett.* **62** 2531

[57] Slichter C P 1990 *Principles of MagneticResonance* (3nd edn.) (Berlin: Springer)

[58] Lange G D, Sar T V D, Blok M, Wang Z H, Dobrovitski V and Hanson R 2012 *Sci. Rep.* **2** 382

[59] Mamin H J, Sherwood M H and Rugar D 2012 *Phys. Rev. B* **86** 195422

[60] Shi F Z, Zhang Q, Wang P F, Sun H B, Wang J R, Rong X, Chen M, Ju C Y, Reinhard F, Chen H, Wrachtrup J, Wang J F and Du J F 2015 *Science* **347** 1135

[61] Mannini M, Pineider F, Sainctavit P, Danieli C, Otero E, Sciancalepore C, Talarico A M, Arrio M A, Cornia A, Gatteschi D and Sessoli R 2009 *Nat. Mater.* **8** 194

[62] Santini P, Carretta S, Troiani F and Amoretti G 2011 *Phys. Rev. Lett.* **107** 230502

[63] Müller A and Döring J 1988 *Angew. Chem. Int. Ed. Engl.* **27** 1721

[64] Yang J H, Wang Y, Wang Z X, Rong X, Duan C K, Su J H and Du J F 2012 *Phys. Rev. Lett.* **108** 230501

[65] Rabl P, Cappellaro P, Dutt M G, Jiang L, Maze J and Lukin M D 2009 *Phys. Rev. B* **79** 041302

[66] Cai J, Naydenov B, Pfeiffer R, McGuinness L P, Jahnke K D, Jelezko F, Plenio M B and Retzker A 2012 *New. J. Phys.* **14** 113023

[67] Fanchini F, Hornos J and Napolitano R D J 2007 *Phys. Rev. A* **75** 022329

[68] Chaudhry A Z and Gong J B 2012 *Phys. Rev. A* **85** 012315

[69] Bermudez A, Jelezko F, Plenio M and Retzker A 2011 *Phys. Rev. Lett.* **107** 150503

[70] Xu X K, Wang Z, Duan C K, Huang P, Wang P F, Wang Y, Xu N Y, Kong X, Shi F Z, Rong X and Du J 2012 *Phys. Rev. Lett.* **109** 070502

[71] Khodjasteh K and Viola L 2009 *Phys. Rev. Lett.* **102** 080501

[72] Khodjasteh K, Lidar D A and Viola L 2010 *Phys. Rev. Lett.* **104** 090501

[73] West J R, Lidar D A, Fong B H and Gyure M F 2010 *Phys. Rev. Lett.* **105** 230503

[74] Kestner J, Wang X, Bishop L S, Barnes E and Sarma S D 2013 *Phys. Rev. Lett.* **110** 140502

[75] Wang X, Bishop L S, Kestner J, Barnes E, Sun K and Sarma S D 2012 *Nat. Commun.* **3** 997

[76] Rong X, Geng J P, Wang Z X, Zhang Q, Ju C Y, Shi F Z, Duan C K and Du J F 2014 *Phys. Rev. Lett.* **112** 050503

[77] Doherty M W, Manson N B, Delaney P, Jelezko F, Wrachtrup J and Hollenberg L C 2013 *Phys. Rep.* **528** 1

[78] Wrachtrup J 2010 *P. Natl. Acad. Sci. USA* **107** 9479

[79] Van der Sar T, Wang Z, Blok M, Bernien H, Taminiau T, Toyli D, Lidar D, Awschalom D, Hanson R and Dobrovitski V 2012 *Nature* **484** 82

[80] Jacques V, Neumann P, Beck J, Markham M, Twitchen D, Meijer J, Kaiser F, Balasubramanian G, Jelezko F and Wrachtrup J 2009 *Phys. Rev. Lett.* **102** 057403

[81] Nielsen M A 2002 *Phys. Lett. A* **303** 249

[82] De Raedt H, Barbara B, Miyashita S, Michielsen K, Bertaina S and Gambarelli S 2012 *Phys. Rev. B* **85** 014408

[83] Wimperis S 1994 *J. Magn. Reson. Ser. A* **109** 221

[84] Bando M, Ichikawa T, Kondo Y and Nakahara M 2012 *J. Phys. Soc. Jpn.* **82** 014004

[85] Rong X, Geng J P, Shi F z, Liu Y, Xu K B, Ma W C, Kong F, Jiang Z, Wu Y and Du J F 2015 *Nat. Commun.* **6** 8748

[86] Knill E, Leibfried D, Reichle R, Britton J, Blakestad R, Jost J, Langer C, Ozeri R, Seidelin S and Wineland D 2008 *Phys. Rev. A* **77** 012307

[87] Khaneja N, Reiss T, Kehlet C, Schulte-Herbrüggen T and Glaser S J 2005 *J. Magn. Reson.* **172** 296

[88] Fowler A G, Mariantoni M, Martinis J M and Cleland A N2012 *Phys. Rev. A* **86** 032324

[89] Carlini A, Hosoya A, Koike T and Okudaira Y 1998 *Phys. Rev. Lett.* **96** 060503

[90] Carlini A, Hosoya A, Koike T and Okudaira Y 2007 *Phys. Rev. A* **75** 042308

[91] Rezakhani A, Kuo W J, Hamma A, Lidar D and Zanardi P 2009 *Phys. Rev. Lett.* **103** 080502

[92] Carlini A, Hosoya A, Koike T and Okudaira Y 2011 *J. Phys. A. Math. Theor.* **44** 145302

[93] Carlini A and Koike T 2012 *Phys. Rev. A* **86** 054302

[94] Carlini A and Koike T 2013 *J. Phys. A. Math. Theor.* **46** 045307

[95] Wang X, Allegra M, Jacobs K, Lloyd S, Lupo C and Mohseni M 2015 *Phys. Rev. Lett.* **114** 170501

[96] Geng J P, Wu Y, Wang X T, Xu K B, Shi F Z, Xie Y J, Rong X and Du J F 2006 *Phys. Rev. Lett.* **117** 170501

[97] Nielsen M A and Chuang I L 2000 *Quantum Computation and Quantum Information*, 2nd edn. (India: Cambridge University Press)

[98] Farhi E, Goldstone J, Gutmann S and Sipser M 2000 arXiv: 0001106 [quant-ph]

[99] Mizel A, Lidar D A and Mitchell M 200 7*Phys. Rev. Lett.* **99** 070502

[100] Knuth D E 1997 *The Art of Computer Programming Volume 2: Seminumerical Algorithms*, 3rd edn. (Massachusetts: Addison-Wesley Longman Publishing)

[101] Vandersypen L, Lidar D A and Mitchell M 2001 *Nature* **414** 883

[102] Lu C, Browne D E, Yang T and Pan J W 2007 *Phys. Rev. Lett.* **99** 250504

[103] Lanyon B, Weinhold T, Langford N, Barbieri M, James D, Gilchrist A and White A G 2007 *Phys. Rev. Lett.* **99** 250505

[104] Politi A, Mattthews J C and O Brien J L 2009 *Science* **325** 1221

[105] Martin-Lopez E, Laing A, Lawson T, Lavarez R, Zhou X and O Brien J L 2012 *Nat. Photon.* **6** 773

[106] Lucero E, Barends R, Chen Y, Kelly J, Mariantoni M, Megrant A, O Malley P, Sank D, Vainsencher A, Wenner J, White T, Yin Y, Cleland A N and Martinis J M 2012 *Nat. Phys.* **8** 723

[107] Monz T, Digg D, Martinez E A, Brandl M F, SChindler P, Rines R, Wang S X, Chuang I L and Blatt R 2016 *Science* **351** 1070

[108] Xu N Y, Zhu J, Lu DW, Zhou X Y, Peng X H and Du J F 2012 *Phys. Rev. Lett.* **108** 130501

[109] Peng X H, Liao Z y, Xu N Y, Qin G, Zhou X Y, Suter D and Du J F 2008 *Phys. Rev. Lett.* **101** 250405

[110] Burges C J 2002 *Micros. Res. Tech. Rep.* **1** 19

[111] Xu K B, Xie T Y, Li Z K, Xu X K, Wang M Q, Ye X Y, Kong F, Geng J P, Duan C K, Shi F Z and Du J F 2017 *Phys. Rev. Lett.* **118** 130504

[112] Koehl W F, Buckley B B, Heremans F J, Calusine G and Awschalom D D 2011 *Nature* **479** 84

[113] Pla J J, Tan K Y, Dehollain J P, Lim W H and Morton J J L 2013 *Nature* **496** 334

[114] Yin C, Rancic M, de Boo G G, Stavrias N, McCallum J C, Sellars M J and Rogge S 2013 *Nature* **497** 91

[115] Heisenberg W 1927 *Zeitschrift für Physik* **43** 172

[116] Kennard E H 1927 *Zeitschrift für Physik* **44** 326

[117] Robertson H P 1929 *Phys. Rev.* **34** 163

[118] Schrödinger E, Zum Heisenbergschen Unschärfeprinzip Z and Preuss Akad Wiss S 1930 *Phys.-Math. Klasse.* **19** 296

[119] Busch P, Heinonen T and Lahti P 2007 *Phys. Rep.* **452** 155

[120] Busch P, Lahti P and Werner R F 2013 *Phys. Rev. Lett.* **111** 160405

[121] Busch P, Lahti P and Werner R F 2014 *Phys. Rev. A* **89** 012129

[122] Busch P, Lahti P and Werner R F 2014 *Rev. Mod. Phys.* **86** 1261

[123] Buscemi F, Hall M J W, Ozawa M and Wilde M M 2014 *Phys. Rev. Lett.* **112** 050401
[124] Sulyok G, Sponar S, Demirel B, Buscemi F, Hall M J W, Ozawa M and Hasegawa Y 2015 *Phys. Rev. Lett.* **115** 030401
[125] Ma W C, Ma Z H, Wang H Y, Chen Z H, Liu Y, Kong F, Li Z, Peng X H, Shi M, Shi F Z, Fei S M and Du J F 2016 *Phys. Rev. Lett.* **116** 160405
[126] Zhang F and Li Y 2018 *Chin. Phys. B* **27** 090301
[127] Ozawa M 2003 *Phys. Rev. A* **67** 042105
[128] Ozawa M 2003 *Int. J. Quantum Inform.* **01** 569
[129] Ozawa M 2004 *Phys. Lett. A* **320** 367
[130] Hall M J W 2004 *Phys. Rev. A* **69** 052113
[131] Branciard C 2013 *P. Natl. Acad. Sci. USA* **110** 6742
[132] Branciard C 2014 *Phys. Rev. A* **89** 022124
[133] Weston M M, Hall M J W, Palsson M S, Wiseman H M and Pryde G J 2013 *Phys. Rev. Lett.* **110** 220402
[134] Erhart J, Sponar S, Sulyok G, Badurek G, Ozawa M and Hasegawa Y 2012 *Nat. Phys.* **8** 185
[135] Sulyok G, Sponar S, Erhart J, Badurek G, Ozawa M and Hasegawa Y 2013 *Phys. Rev. A* **88** 022110
[136] Rozema L A, Darabi A, Mahler D H, Hayat A, Soudagar Y and Steinberg A M 2012 *Phys. Rev. Lett.* **109** 100404
[137] Baek S Y, Kaneda F, Ozawa M and Edamatsu K 2013 *Sci. Rep.* **3** 2221
[138] Ringbauer M, Biggerstaff D N, Broome M A, Fedrizzi A, Branciard C and White A G 2014 *Phys. Rev. Lett.* **112** 020401
[139] Kaneda F, Baek S Y, Ozawa M and Edamatsu K 2014 *Phys. Rev. Lett.* **112** 020402
[140] Di Lorenzo A 2013 *Phys. Rev. Lett.* **110** 120403
[141] Dressel J and Nori F 2014 *Phys. Rev. A* **89** 022106
[142] Korzekwa K, Jennings D and Rudolph T 2014 *Phys. Rev. A* **89** 052108
[143] Busch P, Heinonen T and Lahti P2004 *Phys. Rev. A* **320** 261
[144] Werner R F 2004 *Quantum Inform. Comput.* **4** 546
[145] Li J L and Qiao C F 2015 *Sci. Rep.* **5** 12708
[146] Coles P J, Berta M, Tomamichel M and Wehner S2017 *Rev. Mod. Phys.* **89** 015002
[147] Chen B and Fei S M 2015 *Sci. Rep.* **5** 14238
[148] Abbott A A, Alzieu P L, Hall M J W and Branciard C 2016 *Mathematics* **4** 8
[149] Chen B, Fei S M and Long G L 2016 *Quantum Inform. Process.* **15** 2639
[150] Chen B, Cao N P, Fei S M and Long G L 2016 *Quantum Inf. Process.* **15** 3909
[151] Busch P 1986 *Phys. Rev. D* **33** 2253
[152] Yu S, Liu N l, Li L and Oh C H 2010 *Phys. Rev. A* **81** 062116
[153] Kechrimparis S and Weigert S 2014 *Phys. Rev. A* **90** 062118
[154] Lars D, Rene S and Reinhard F W 2015 *New J. Phys.* **17** 093046
[155] Hofmann H F and Takeuchi S 2003 *Phys. Rev. A* **68** 032103